Advanced Powder Technology 29 (2018) 2003–2018

Contents lists available at ScienceDirect

Advanced Powder Technology

journal homepage: www.elsevier.com/locate/apt

Original Research Paper

Numerical investigation of dilute aerosol particle transport and deposition in oscillating multi-cylinder obstructions

Shi Tao [a], Haolong Zhang [a], Zhaoli Guo [a,b,*], Lian-Ping Wang [a,c]

[a] State Key Laboratory of Coal Combustion, School of Energy and Power Engineering, Huazhong University of Science and Technology, Wuhan 430074, Hubei, China
[b] Beijing Computational Science Research Center, Beijing 100084, China
[c] Department of Mechanical Engineering, University of Delaware, Newark, DE 19716-3140, USA

ARTICLE INFO

Article history:
Received 2 November 2017
Received in revised form 20 March 2018
Accepted 6 May 2018
Available online 17 May 2018

Keywords:
Particle-laden flow
Filtration
Collection efficiency
Oscillating fibers
Iterative IB-LBM

ABSTRACT

The transport and deposition of aerosol particles through a fibrous filter is encountered in many natural and industrial processes. As the filtration performance for a stationary filter has been extensively studied in the literature, the present work focuses on the effect of fiber oscillation in a filter where the fibers are allowed to vibrate periodically. The transport and deposition of dilute aerosol particles in such a system is simulated using an efficient numerical model, where an iterative immersed-boundary lattice Boltzmann method is applied to solve the background flow with finite-size moving fibers, and the motion of aerosol particles is then tracked by a one-way coupling Lagrangian approach. In the present scheme, the no-slip boundary condition at the fiber surface can be exactly enforced with an iterative approach and the numerical stability is improved by adopting the MRT collision model. After the model validation in the two special cases of flow over an oscillating fiber in a quiescent fluid and particle capture by a stationary fiber, the filtration performance of an oscillating multi-fiber filter is investigated to study the effects of fiber number, arrangement and vibration mode. It is found that the oscillating motion of fiber has significant influence on the filtration performance. For a single fiber, with larger oscillation amplitude, the distribution ranges of the release position and impact angle of captured particles both increase. On the other hand, a larger fiber oscillation frequency tends to reduce the width of release position but increase the width of impact angle of deposited particles. Furthermore, the collection efficiency is found to be linearly related to the oscillation amplitude or frequency. For multiple fibers, the collection efficiency always increases with larger fiber number, but it is a non-monotonic function of the arrangement parameters, i.e., the longitudinal and transverse spacings, and the vibration parameters such as the amplitude, frequency and vibration mode. It is interesting to find that the in-phase mode can usually lead to excellent collection efficiency.

1. Introduction

The transport and deposition of airborne particles is encountered in a wide range of natural and industrial processes, such as the filtration, combustion and chip fabrication. In particular, one of the most attracting topics is the investigation of the fine particle removal from air [1–3]. An increasing body of works has revealed the adverse health effects of inhaled sub-micron particles [4], as a result of growing environmental concern and stricter regulatory legislation, both of which will continue to promote interest in the development of advanced particle removal technology. The commonly used dedusting methods could be roughly separated into four categories, i.e., mechanical impact from gravitational settling and cyclone separation, electrostatic precipitation, wet scrubbing and fibrous filtration [1]. Generally, filter made from the fibers with various kinds of materials is one of the most popular dedusting apparatus, due to the advantages of low cost, simple construction and high collection efficiency. For further improving the collection efficiency, there are also many new precipitators which combine the electrostatic and/or wet scrubbing technologies with the fibrous filter nowadays, such as the wet vibrating grid precipitator (WVGP) [5,6].

The flow through a fibrous filter is very complicated due to the coexistence and interactions among fluid flow, finite-size fibers, and small suspended particles. Many works have been devoted

* Corresponding author at: State Key Laboratory of Coal Combustion, School of Energy and Power Engineering, Huazhong University of Science and Technology, Wuhan 430074, Hubei, China.
E-mail address: zlguo@hust.edu.cn (Z. Guo).

https://doi.org/10.1016/j.apt.2018.05.007
0921-8831/

to study such filtration process. Brandon et al. [7] carried out numerical investigation of the particle deposition on a square cylinder placed in a channel flow. The effects of Stokes number *St*, Reynolds number *Re*, density ratio *S* (to be defined more precisely in Section 2) and the driving forces for the particle dispersion and deposition were considered. Yao et al. [8] used the spectral-element method to study the different patterns of particle dispersion in the wake of a circular cylinder. Jafari et al. [9] investigated the particle dispersion and deposition in a channel with a square cylinder obstruction using the lattice Boltzmann method. The ranges of *Re* and particle diameter d_p are, 120–200 and 0.01–10 μm, respectively. It was found that the Brownian diffusion affected the deposition rate of ultrafine particles on the front and back sides of the block, and the motion of particles behind the obstacle was greatly influenced by the vortex shedding. Haugen et al. [10] considered the particle impaction on a cylinder in a cross-flow as function of *St* and *Re*. The immersed boundary method was applied to solve the flow, and for the motion of particles only the drag force was taken into account. A new Stokes number was proposed to better scale the results. Particle impaction on the back side of the cylinder was observed, and this phenomenon was strongly dependent on the flow *Re*.

Results of the studies mentioned above have great implications both theoretically and practically for the development of high performance filter. However, it can be found that they are mostly restricted to a single fiber which may not very representative of a real fibrous filter. To overcome this defect, some researchers investigated the filtration performance of multi-fiber filter. Shou et al. [11] derived analytically the collection efficiency of filter where the fibers were distributed randomly. Liu et al. [12] studied the particle-laden flow past the multi-fiber filter and shown that the collection efficiency could not be represented by the single-fiber models. Lin et al. [13] focused on the multiple staggered fibrous filters. The influence of the fiber separation ratio in longitudinal and transverse directions on the filtration process was determined. Recently, Li et al. [14] used the numerical approach in an effort to optimize the filtration performance of a multi-fiber filter, which was composed of fibers with different diameter and structure. However, the flow *Re* in the filter was low, i.e., $Re < 1.0$ so that the inertial effect of flow could not be addressed. Shou et al. [15] also considered fibers with different sizes, and the fibers being interlaced in the filter.

Although the filtration of airborne particles by both single and multiple fibers has been studied in the past, most studies assumed that fibers are stationary. Therefore, relatively little is known concerning the influence of fiber movement on the filtration performance [16,17]. Khorasanizade et al. [18] used the smoothed particle hydrodynamics (SPH) method to study the dispersion of particles in the wake of a moving plate. For a flat plate collector, Holmes et al. [19] observed experimentally that both plunge and torsional oscillations could increase the collection efficiency. In the study of particle sampling by Price et al. [20], it was found that moving collectors could offer significant advantages over stationary one. Utilizing the fluid-structure interaction approach, Ryan et al. [21] investigated the influence of moving walls to mimic the realistic lung behavior on the deposition of respiratory aerosol. Substantial different results were obtained in comparison to those from stationary geometry with even imposed oscillating flows. Krick et al. [22] considered that the gas flow could cause the oscillation motion of a circular cylinder for higher flow *Re*. In the background of anemophilous pollination, the authors investigated the particle capture by an elastically mounted cylinder at *Re* as large as 3309 with a *St* range of 0.01–5.0. It should be noted that the flow *Re* may be too large for a fibrous filter and at the same time only one fiber is involved. Recently, Liu et al. [23] and Chen et al. [24,25] studied the performance of gas-solid separation for moving granular bed.

For the fibrous filtration, numerical approach has played an important role in solving the complicated flow resulting from blocking of fibers and resulting flow interactions. In the past few years, the lattice Boltzmann method (LBM) has been developed into a widely-used flow solver for the Navier-Stokes equations [26,27]. The method has also been applied to general particle-laden flows [28–30]. In LBM, mainly there are two schemes used to treat the no-slip boundary condition, i.e., the simple or interpolated bounce-back (BB) rule [31], and the immersed boundary (IB) method [32,33]. The flow field obtained by the BB-type method could have serious unphysical fluctuations when handling the moving boundaries [34]. This problem has been actively investigated in recent years and the sources of force oscillation have been partially identified and removed [35]. On the other hand, the IB scheme could largely avoid this problem, due to the help of local regularization or smoothing, and is therefore adopted in the present work. On the other hand, an iterative algorithm [36] is introduced into the standard IB method to solve the problem of streamline penetration [32], namely, the inaccurate implementation of the no-slip boundary condition. Furthermore, the MRT (multiple-relaxation time) collision model is adopted for substituting the commonly used LBGK (lattice Bhatnagar-Gross-Krook) model in LBM to improve the computational stability [26]. The iterative IB-LBM is then established and is to be validated in the following to have good performance in simulation of flow with moving boundaries. As for the motion of small aerosol particles, it is usually tracked by the Lagrangian approach [37].

In this work, a numerical model coupling the iterative IB-LBM for flow through fibers with the Lagrangian approach for tracking the aerosol particles is developed and used to investigate the filtration process of the oscillating multi-fiber filter. The present simulation is served as a practical analogy to the WVGP [5,6,38], where the effects of fiber number, arrangement and vibration mode are investigated. The remaining part of this paper is organized as follows. A statement of the problem is provided in Section 2. The numerical model including the lattice Boltzmann method, immersed boundary scheme, and the Lagrangian approach is introduced and validated in Section 3. In Section 4, we present the simulation results for the examination of the effects of fibers number, arrangement and vibration mode. Finally, conclusions are summarized in Section 5.

2. Problem description

The geometric model of the present fibrous filtration system for airborne particles is sketched in Fig. 1. The gas has a temperature *T*, density ρ_f and dynamic viscosity μ, and entrains a dilute concentration of particles with the density ρ_p and diameter d_p. The flow is assumed to be not affected by the aerosol particles due to the assumption of very low mass loading; Only the trajectories of the aerosol particles are driven by the flow (i.e., one-way coupling); Particle-particle interactions are also neglected (Those assumptions may generally hold for mass loading less than 8‰ [28]). The particle-laden flow is fed towards an array of oscillating finite-size circular fibers. The flow Reynolds number *Re* is fixed at 100, defined as $Re = \rho_f U_0 D/\mu$ where U_0 is the velocity of free stream, and *D* is the diameter of fiber. Hence, the present model falls into the range of inertial fibrous filters [2]. The physical and corresponding computational parameters of the gas, particle and fiber are given in Table 1. It is known that the deduced stream velocity, U_0, is high (up to tens of m/s) which is an important feature for the inertial fibrous filters [2,39,40]. The fibrous filter is semi-infinite in the *y*-direction. Therefore, to decrease the computational effort in simulations, it is reasonable to make use of the periodic boundaries to just consider a row of fibers [13], as shown

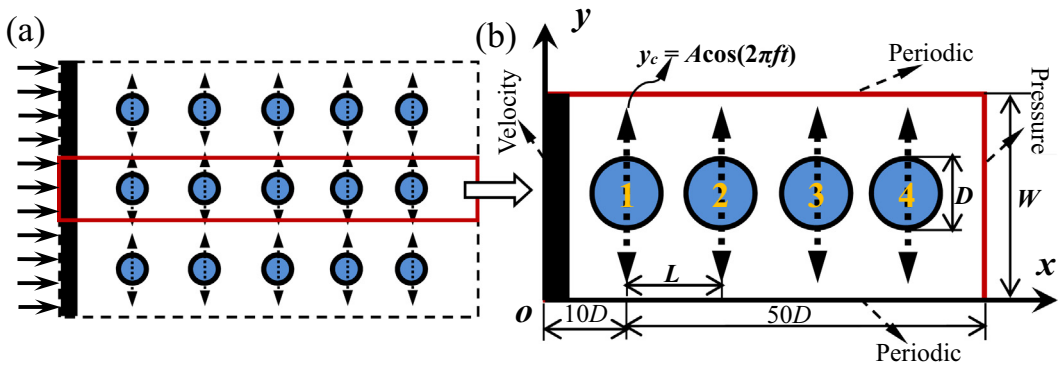

Fig. 1. Schematic of the oscillating multi-fiber filter.

Table 1
The physical and corresponding computational parameters of the gas, particle and fiber. τ_s is the relaxation time related to the kinematic viscosity and δ_t is the time step of LBM.

Variables	Physical	Computational
Fluid density	1.205 kg/m^3	1.0
Fluid temperature	293.15 K	—
Fluid viscosity	1.81×10^{-5} Pa s	$(\tau_s - 0.5)\delta_t/3$
Particle density	2500 kg/m^3	2500/1.205
Particle diameter	$8.07 \times 10^{-8} \sim 1.04 \times 10^{-6}$ m	—
Fiber diameter	5.0×10^{-5} m	60

in Fig. 1(b). Note that the fibers are arranged uniformly with the longitudinal and lateral spacings, L and W respectively, and are in harmonic oscillation in the transverse direction. The fiber motion is assumed to be described by $y_c = \pm A\cos(2\pi ft)$, where A and f are the oscillation amplitude and frequency of fiber, respectively. Note that this passive oscillation can be analogy to the vortex induced vibration (VIV) of fibers which is the case in some real applications.

Apart from Re, a set of dimensionless parameters, i.e., the total number of fibers N, Stokes number St, length ratio L/D, width ratio W/D, amplitude ratio A/D, frequency ratio f/f_s, and the density ratio S are established for the present particle-laden flows. The range of N is from 1 to 7. St, defined in Eq. (23), is 0.06–10 for the particle size range considered. The two separation ratios, L/D = 2–6 and W/D = 2–4 are for the arrangement of fibers. A/D = 0.1–0.5 and f/f_s = 0.6–2.5 are the control parameters for the vibration of a single fiber, where $f_s = Str/\tau_f$ is the frequency of von Karman eddies in the single stationary fiber case. For Re = 100 in this work, the Strouhal number Str ($Str = fD/U_0$) is calculated using the iterative IB-LBM to be 0.167, consistence with those in literature [36]; the response time of fluid τ_f is defined in Eq. (22). The density ratio $S = \rho_p/\rho_f$ equals to 2500/1.205. As multiple fibers involved, two of them may oscillate in phase as well as anti-phase. Hence, four vibration modes are considered, as shown in Fig. 22. It should be noted that, unless otherwise stated, the motion of fibers is in Mode 1 (Fig. 22 (a)). In the simulations, after the flow reaches a time-periodic state, the particles are introduced into the flow domain randomly at the inlet cross-section, with an initial velocity the same as that of free stream. Once the distance between the particle center and the fiber surface is less than one particle radius, the particle is thought to be captured by the fiber and then removed from the flow field. This scenario can be the case for some wet fibrous filters, where particles adhere to the fibers and are then entrained by the liquid film to the sedimentation bank [5,41]. The release position and the impact angle for the captured particle, defined in Fig. 2 are then calculated and recorded.

3. Numerical methodology and validation

3.1. Lattice Boltzmann method for the gas flows

The lattice Boltzmann method (LBM) has been greatly advanced in recent years to be an alternative solver for the viscous flows [26,42,43]. As a kinetic method, LBM has several unique advantages, for instance high efficiency in computation and handling the complex boundaries. In LBM, a set of velocity distribution functions $f_i(\boldsymbol{x}, t)$ at position $\boldsymbol{x}$, time t, and discrete velocity $\boldsymbol{e}_i$, rather than the macroscopic quantities are tracked, which are subject to the lattice Boltzmann equation as

$$f_i(\boldsymbol{x} + \boldsymbol{e}_i\delta_t,\ t + \delta_t) - f_i(\boldsymbol{x},\ t) = \Omega_i(f) + \delta_t \boldsymbol{F}_i,$$
$$i = 0,\ 1,\ \ldots,\ b-1, \tag{1}$$

where $\Omega_i(f)$ denotes the discrete collision operator, $\boldsymbol{F}_i$ the discrete external forcing term, δ_t the time step and b the total number of discrete velocities. Note that the MRT (multi-relaxation-time) collision model is adopted for substituting the generally used LBGK (lattice Bhatnagar-Gross-Krook) model to avoid the unphysical numerical artifact and improve stability [26,42], in which the collision term expressed as

$$\Omega_i(f) = -\sum_j (\boldsymbol{M}^{-1}\boldsymbol{S}\boldsymbol{M})_{ij}(f_j - f_j^{eq}), \tag{2}$$

where $\boldsymbol{M}$ is a $b \times b$ transform matrix, and $\boldsymbol{S}$ is a diagonal relaxation matrix; f_j^{eq} is the equilibrium distribution function which depends on the densityρ, velocity $\boldsymbol{u}$, and temperature T of the gas and is typically defined as [27]

$$f_j^{eq} = \omega_j \rho \left[1 + \frac{\boldsymbol{e}_j.\boldsymbol{u}}{c_s^2} + \frac{(\boldsymbol{e}_j.\boldsymbol{u})^2}{2c_s^4} - \frac{u^2}{2c_s^2}\right], \quad j = 0,\ 1,\ \ldots,\ b-1, \tag{3}$$

where ω_j is the model-dependent weight coefficient, $c_s = \sqrt{RT}$ (R is the gas constant) the lattice sound speed. For isothermal flows, c_s is set to be $c/\sqrt{3}$ with $c = \delta_x/\delta_t$, where δ_x is the lattice spacing (c = 1 in

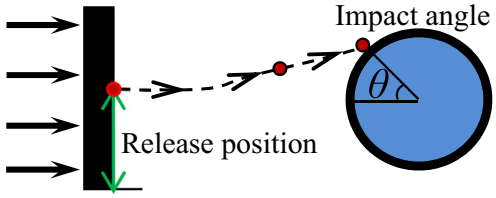

Fig. 2. Particle captured by a fiber with the impact angle and released position.

this paper). For consistency, the forcing term $\boldsymbol{F}_i$ in Eq. (1) should be given by [44]

$$\boldsymbol{F} = \boldsymbol{M}^{-1}(\boldsymbol{I} - \boldsymbol{S}/2)\boldsymbol{M}\overline{\boldsymbol{F}}, \tag{4}$$

where $\boldsymbol{I}$ is the identity matrix, $\boldsymbol{F} = (F_0,\ F_1,\ \ldots,\ F_{b\text{-}1})$ and $\overline{\boldsymbol{F}} = (\overline{F}_0,\ \overline{F}_1,\ \ldots,\ \overline{F}_{b-1})$ with

$$\overline{F}_i = w_i\left[\frac{\boldsymbol{e}_i\cdot\boldsymbol{g}}{c_s^2} + \frac{\boldsymbol{u}\boldsymbol{g} : (\boldsymbol{e}_i\boldsymbol{e}_i - c_s^2\boldsymbol{I})}{c_s^4}\right], \quad i = 0,\ 1,\ \ldots,\ b-1. \tag{5}$$

Here $\boldsymbol{g}$ is the external force per unit volume. Through Chapman-Enskog expansion, the macroscopic fluid density ρ and velocity $\boldsymbol{u}$ can be derived as the zeroth and first order moments of f_i respectively,

$$\rho = \sum_{i=0}^{b-1} f_i, \quad \rho\boldsymbol{u} = \sum_{i=0}^{b-1}\boldsymbol{e}_i f_i + 0.5\delta_t\boldsymbol{g}. \tag{6}$$

The fluid pressure is defined directly as $p = c_s^2\rho$, and the fluid viscosity is related to the relaxation time τ_s for the shear moment as

$$\mu = \rho c_s^2(\tau_s - 0.5)\delta_t. \tag{7}$$

For simplicity and without loss of generality, the D2Q9 model (two dimensions with nine lattice velocities) is employed in this study [27], in which the velocity set and the corresponding weight coefficients are defined as

$$\boldsymbol{e}_i = \begin{cases} (0,\ 0), & i = 0 \\ [\cos(i-1)\pi/4,\ \sin(i-1)\pi/4], & i = 1,\ 2,\ 3,\ 4 \\ \sqrt{2}[\cos(i-1)\pi/4,\ \sin(i-1)\pi/4], & i = 5,\ 6,\ 7,\ 8 \end{cases}. \tag{8}$$

$$\omega_i = \begin{cases} 4/9, & i = 0 \\ 1/9, & i = 1,\ 2,\ 3,\ 4 \\ 1/36, & i = 5,\ 6,\ 7,\ 8 \end{cases}. \tag{9}$$

The transform matrix $\boldsymbol{M}$ is given by [42]

$$\boldsymbol{M} = \begin{bmatrix} 1 & 1 & 1 & 1 & 1 & 1 & 1 & 1 & 1 \\ -4 & -1 & -1 & -1 & -1 & 2 & 2 & 2 & 2 \\ 4 & -2 & -2 & -2 & -2 & 1 & 1 & 1 & 1 \\ 0 & 1 & 0 & -1 & 0 & 1 & -1 & -1 & 1 \\ 0 & -2 & 0 & 2 & 0 & 1 & -1 & -1 & 1 \\ 0 & 0 & 1 & 0 & -1 & 1 & 1 & -1 & -1 \\ 0 & 0 & -2 & 0 & 2 & 1 & 1 & -1 & -1 \\ 0 & 1 & -1 & 1 & -1 & 0 & 0 & 0 & 0 \\ 0 & 0 & 0 & 0 & 0 & 1 & -1 & 1 & -1 \end{bmatrix} \tag{10}$$

and the relaxation matrix is

$$\boldsymbol{S} = diag(\tau_\rho, \tau_e, \tau_\varepsilon, \tau_d, \tau_q, \tau_d, \tau_q, \tau_s, \tau_s)^{-1}. \tag{11}$$

where (τ_ρ, τ_d) and the remaining ones are the relaxation times for conserved and non-conserved moments which can take arbitrary values and should be set greater than 0.5, respectively. The values of the relaxation times used in the simulations are presented in Table 2.

3.2. Immersed boundary method for the moving fiber surface

The no-slip boundary condition on the surface of a fiber is implemented by the immersed boundary (IB) method, which is an efficient scheme for moving boundary problems. The IB method was first proposed by Peskin et al. [45] to solve flow in or through cardiac valves. Subsequently, Feng et al. [32] combined it with LBM and hence developed the so-called IB-LBM where LBM is used for the flows and IB method is used to treat the moving boundaries. In the IB scheme, the no-slip boundary of body is discretized into a set of Lagrangian points $\boldsymbol{X}$, as shown in Fig. 3. Each point is used to support a local external force. Such force will be distributed to the ambient Eulerian points $\boldsymbol{x}$, called as forcing process. In this manner, the fluid senses the existence of the immersed physical boundary, and the no-slip boundary condition is replaced by a localized force field.

We should first calculate the local force at the Lagrangian point. There are several force schemes available in the literature [46]. The direct forcing model, derived directly from the momentum equation and including no empirical parameters [46] is chosen in this work, which gives the force as

$$\boldsymbol{G} = 2\rho_f\frac{\boldsymbol{U} - \boldsymbol{u}^*}{\delta_t}, \tag{12}$$

where $\boldsymbol{U}$ is the imposed velocity and $\boldsymbol{u}^*$ the fluid velocity before forcing, both at the position of a Lagrangian point. The $\boldsymbol{u}^*$ can be obtained from the velocities at the Eulerian points through the discrete delta function $D(\boldsymbol{x} - \boldsymbol{X})$ as

$$\begin{aligned} &D(\boldsymbol{x} - \boldsymbol{X}) = \frac{1}{\delta_x^2}\delta(x - x_l)\delta(y - y_l), \\ &(a)\ \delta(r) = \begin{cases} 1 - |r|, & |r| \leqslant 1, \\ 0, & |r| > 1; \end{cases} \\ &(b)\ \delta(r) = \begin{cases} \frac{1}{3}\left(1 + \sqrt{1 - 3r^2}\right), & |r| < 0.5, \\ \frac{1}{6}\left(5 - 3|r| - \sqrt{1 - 3(1 - |r|)^2}\right), & 0.5 \leqslant |r| < 1.5, \\ 0, & |r| \geqslant 1.5, \end{cases} \\ &(c)\ \delta(r) = \begin{cases} \frac{1}{4}\left(1 + \cos\left(\frac{\pi|r|}{2}\right)\right), & |r| \leqslant 2, \\ 0, & |r| > 2, \end{cases} \end{aligned} \tag{13}$$

where $\boldsymbol{x} = (x, y)$, $\boldsymbol{X} = (x_l, y_l)$, and (a), (b) and (c) are respectively the 2-, 3- and 4-point interpolation functions plotted in Fig. 4. It can be observed that the function is much flatter and smoother with larger work range. As outlined above, the interpolation function transfers the information between the solid and fluid phases, and hence plays a significant role in the property of momentum conservation (MC) for the IB scheme. Those three functions with different work ranges are considered and will be later evaluated regarding the MC property.

The calculated force is then distributed to the fluid Eulerian points using the same delta function given in Eq. (13) as

$$\boldsymbol{g}(\boldsymbol{x}) = \sum_{\boldsymbol{X}}\boldsymbol{G}(\boldsymbol{X})D(\boldsymbol{x} - \boldsymbol{X}). \tag{14}$$

Looping the above process (obtaining the force at the Lagrangian points and distributing it back to Eulerian grids) for all the Lagrangian points, the standard IB scheme is then implemented.

Table 2
The values of the relaxation times used in the simulations.

τ_ρ	τ_e	τ_ε	τ_d	τ_q	τ_s
1.0	0.9	0.8	1.0	0.88	$0.5 + 3\nu/\delta_t$

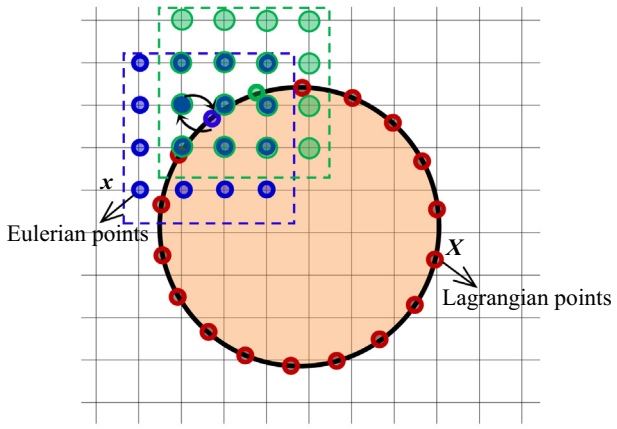

Fig. 3. Immersed boundary scheme for the no-slip boundary condition of moving fiber.

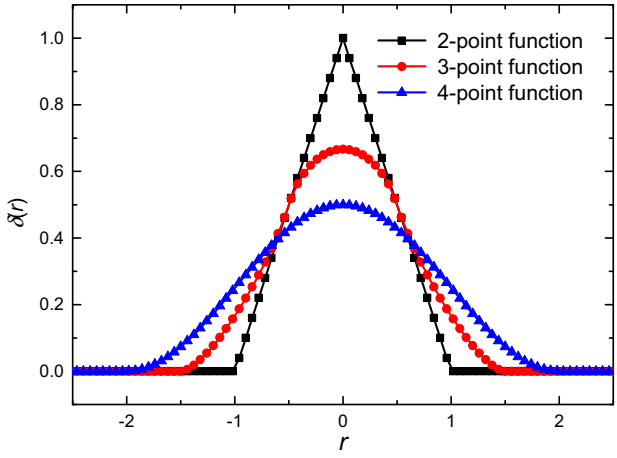

Fig. 4. Interpolation functions with different work ranges.

However, it is found recently that, the no-slip boundary condition is only approximately satisfied in the standard IB method because of the forward/backward interpolation errors, leading to unphysical streamline penetration [36]. To repair this problem, an iterative scheme [36] is introduced in the present study. The iterative algorithm repeats the above forcing procedure multiple times, to gradually force the interpolated velocity $\boldsymbol{u}$ in Eq. (6) towards the boundary velocity $\boldsymbol{U}$. It is found that within a finite number of iterations about 10, the residual error of velocity will be reasonably small. Fig. 5 presents the computational procedure of the present iterative IB-LBM in each time step. Note that for the conventional non-iterative IB-LBM, there is no second loop to reduce the deviation between the interpolated and desired velocities.

3.3. Lagrangian approach for tracking the aerosol particles

The motion of aerosol particle is solved by the Lagrangian approach [37,47]. In this approach, the velocity of particle $\boldsymbol{u}_p$ is governed by the equation of motion as

$$\frac{d\boldsymbol{u}_p}{dt} = \frac{\boldsymbol{F}}{m_p}, \tag{15}$$

where m_p is the particle mass and $\boldsymbol{F}$ is the total force experienced by the particle. As the density ratio is quite high and the mass loading is very low, the primary forces are the viscous drag force $\boldsymbol{F}_D$ and Brownian force $\boldsymbol{F}_B$. The gravity force is neglected in this study for

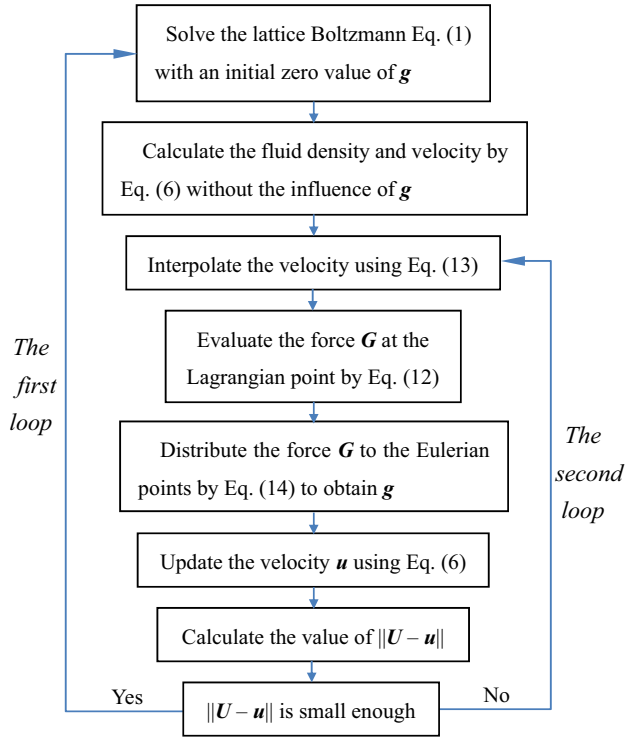

Fig. 5. Flow chart of the computational procedure of the iterative IB-LBM in each time step.

the 2D filtration problem considered, namely, the fibers are assumed to be arranged vertically.

The drag force $\boldsymbol{F}_D$ is described as

$$\boldsymbol{F}_D = \frac{1}{2} C_D \rho_f A |\boldsymbol{u} - \boldsymbol{v}| (\boldsymbol{u} - \boldsymbol{v}) f(C_D, C_c)/C_c, \tag{16}$$

where C_D is the drag coefficient given by [48,49]

$$C_D = \frac{24}{Re_p}(1 + 0.15 Re_p^{0.687}), \quad Re_p \leqslant 800. \tag{17}$$

Here, $Re_p = \rho_f d_p |\boldsymbol{u} - \boldsymbol{v}|/\mu$ is the particle Reynolds number. $A = \pi d_p^2/4$ is the cross-sectional area of the particle. C_c is the Stokes-Cunningham slip correction factor and is expressed as [50]

$$C_c = 1 + 2Kn_p\left[1.142 + 0.558\exp(-0.4995/Kn_p)\right], \tag{18}$$

where $Kn_p = \lambda/d_p$ is the particle Knudsen number, with λ the mean free path of gas (for air at standard condition, $\lambda = 67$ nm). $f(C_D, C_c)$ represents the combined effect of the C_D and C_c [51] and assumes the form of

$$f(C_D, C_c) = \exp\left(1.4067 - 1.5027 Re_p^{0.01803} + 0.00118 Kn_p^{-0.7934} + 0.09905 Re_p Kn_p\right). \tag{19}$$

For Stokes flow ($Re_p << 1$) and relative large particle ($Kn_p << 1$), Eqs. (17) and (18) collapse to $C_D = 24/Re_p$ and $C_c = 1$ respectively, and Eq. (16) can then be rewritten as

$$\boldsymbol{F}_D = \frac{m_p}{\tau_p}(\boldsymbol{u} - \boldsymbol{v}), \tag{20}$$

where τ_p is the particle response time derived as

$$\tau_p = \frac{\rho_p d_p^2}{9\mu}, \tag{21}$$

Comparing the particle response time τ_p with the time scale of the carrier flow,

$$\tau_f = \frac{D}{U_0}, \tag{22}$$

the Stokes number is then defined

$$St = \frac{\tau_p}{\tau_f} = \frac{\rho_p d_p^2 U_0}{18\mu D}, \tag{23}$$

Eq. (23) can be rewritten as

$$d_p = 3D\sqrt{\frac{2St}{S\,Re}}. \tag{24}$$

The Brownian force $\boldsymbol{F}_B$ represents the effect of the random imparted momentum from the gas molecules, and, in the continuum regime, is modeled as the Gaussian white noise as [52]

$$\boldsymbol{F}_B = \begin{pmatrix}\zeta_x\\ \zeta_y\end{pmatrix}\sqrt{\frac{6\pi k_B T\mu D}{\Delta t C_c}} = m_p\begin{pmatrix}\zeta_x\\ \zeta_y\end{pmatrix}\sqrt{\frac{216\mu k_B T}{\pi\rho_p^2 d_p^5 \Delta t C_c}}, \tag{25}$$

where ζ_x and ζ_y are random numbers with a zero mean and a unit variance, k_B is the Boltzmann constant and T the gas temperature.

With the forces $\boldsymbol{F}_D$ and $\boldsymbol{F}_B$ described as above, the particle velocity and displacement can then be explicitly updated through integrating the Eq. (15) and are given as

$$\boldsymbol{u}_p^{n+1} = \boldsymbol{u}_p^n \exp\left(-\frac{\Delta t}{\tau_p}\right) + (\boldsymbol{u} + \boldsymbol{F}_B\tau_p)\left[1 - \exp\left(-\frac{\Delta t}{\tau}\right)\right], \tag{26a}$$

$$\boldsymbol{x}_p^{n+1} = \boldsymbol{x}_p^n + (\boldsymbol{u}_p^n - \boldsymbol{u})\left[1 - \exp\left(-\frac{\Delta t}{\tau_p}\right)\right]\tau_p + \boldsymbol{u}\Delta t + \left\{\Delta t - \left[1 - \exp\left(-\frac{\Delta t}{\tau_p}\right)\right]\tau_p\right\}\boldsymbol{F}_B\tau_p. \tag{26b}$$

where the superscript n and $n+1$ indicate the present and next time moments, respectively. It is known that the particles are generally not exactly at the Eulerian point. Hence, the velocity of fluid $\boldsymbol{u}$ in Eq. (26) is to be obtained by the bilinear interpolation scheme.

3.4. Model validation

For validation of the numerical approach, i.e., the iterative IB-LBM for the gas flow and the Lagrangian approach for the particles, two flow problems are respectively simulated including a fiber oscillating in a quiescent fluid and the particle-laden flow around a single fiber. In the simulations, the 4-point interpolation function is used unless otherwise specified.

3.4.1. An oscillating fiber in a quiescent fluid

A single fiber oscillating in a stationary fluid is considered to test the iterative IB-LBM for the flow simulation with moving boundary. This problem has been studied experimentally and numerically by many researchers [53,54]. The computational domain is $40D \times 30D$. A circular fiber with diameter $D = 40$ lattices initially locates at the center of the domain, and then undergoes harmonic oscillation in the x-direction. The motion of the fiber center is given by $x(t) = -A\sin(2\pi ft)$, where A is the amplitude and f is the frequency of fiber. Two control parameters, the Reynolds number and the Keulegan-Carpenter number, in this problem are defined as $Re = \rho_f U_{\max} D/\mu$ and $KC = U_{\max}/fD$ where $U_{\max} = 2\pi fA$ is the maximum velocity of the fiber. In the simulation, Re and KC are set to be 100 and 5, respectively. For this parameter set, it is reasonable to believe that the flow is to be two-dimensional [55]. The Neumann boundary condition of $\boldsymbol{n}.\nabla f_i = 0$ ($\boldsymbol{n}$ the unit vector normal to the boundary) is applied to the outer boundaries of the domain.

The interpolation method plays a significant role in the IB scheme [56]. To explore such influence, the change of momentum dM_t for the three types of interpolation functions with different work ranges (given by Eq. (13)) is first evaluated and presented in Fig. 6, where M_t is the total momentum of the fluid and cylinder, and nondimensionalized by the maximum momentum of cylinder $M_{s,\max} = \pi\rho U_{\max} D^2/4$. The value of momentum change fluctuates around zero with fairly small amplitude (less than 0.2%). Therefore, it is found that the interpolation method has little influence and momentum conservation is generally satisfied in the present simulations. The streamlines around the oscillating fiber are further shown in Fig. 7. Note that we fix the reference frame on the oscillating fiber (only) in this figure. It is observed that the unphysical phenomenon of streamline-penetration [32] is avoided by the present iterative IB-LBM. Fig. 8 presents the velocity profiles in the vertical cross-section at four locations $x = -0.6D$, 0, $0.6D$ and $1.2D$, and for two phase angles $\phi = 210°$ and 330°, where the coordinate is relative to the equilibrium position of the fiber ($20D$, $15D$), and $\phi = ft \times 360°$. It can be found that the present results have a good agreement with the experiment and numerical data [53,54]. This indicates that the present multi-direct-forcing IB-LBM can accurately predict the complex flow field, which is required for tracking the particles using the Lagrangian approach.

3.4.2. Particle capture by a stationary fiber

To validate the Lagrangian approach for the transport of particle, the particle-laden flow around a stationary circular fiber is investigated. The computational domain is $40D \times 6D$. The fiber locates at a distance of $10D$ from the inlet. The flow Re is fixed at 100, defined as $Re = \rho_f U_0 D/\mu$ where U_0 is the velocity of free stream. The density ratio $S = \rho_p/\rho_f$ is 1000. A longer box is used here which is found to be enough to obtain domain-independent results of collection efficiency and impact angle. The other parameters are set to be the same as those in Ref. [10]. Periodic boundary condition for both the fluid and particle is used in the transverse direction.

Fig. 9 depicts the collection efficiency and the maximum impact angle as functions of St. The numerical results from Haugen et al. [10] and experimental fitting curve from Muhr [57] are included for comparison. Good agreement can be found between the present results and those in literature [10,57].

4. Results and discussion

In this section, the particle-laden flows through a line of oscillating fibers are simulated. Three effects for the control of the

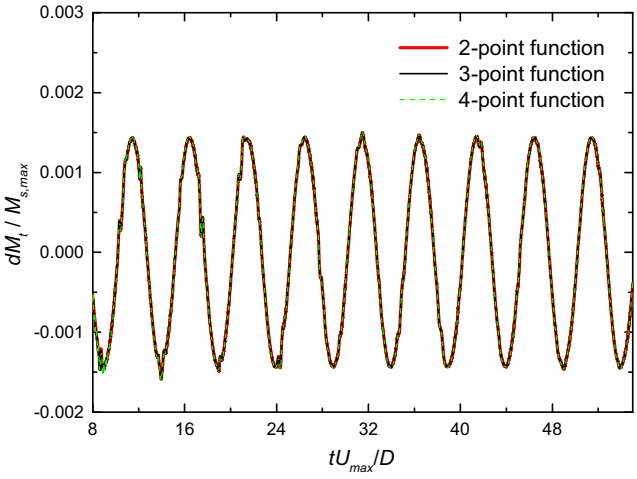

Fig. 6. The change of the total momentum with time for three types of interpolation functions.

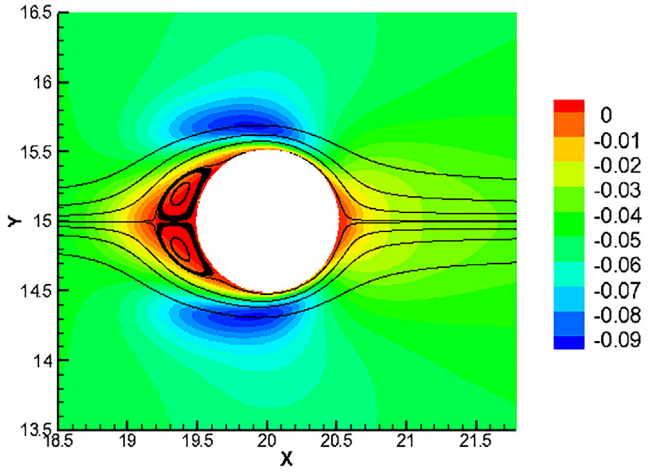

Fig. 7. Streamlines and contour of the *x*-component velocity around the oscillating fiber with the reference frame fixed at the fiber center.

multi-fiber filter are considered, i.e., the fiber number N (from 1 to 7), the fiber arrangement parameters (separation ratios in the longitudinal and transverse directions as L/D and W/D) and the fiber vibration parameters (amplitude, frequency and vibration mode), which are thought to have great influence on the filtration performance.

4.1. Effect of fiber number

4.1.1. A single fiber

We first examine the effect of fiber number. In particular, as the base case of multi-fiber filter, the case of a single fiber is investigated in detail. In the simulations, the transverse spacing is fixed at $W/D = 3$ and the longitudinal spacing L/D is not meaningful for this situation. The Stokes numbers are set to be $St = 0.2$, 1.0 and 5.0. The A/D and f/f_s vary in the ranges of 0.1 –0.4 and 0.6 –2.5, respectively. Together with the Re fixed at 100, under those parameters the flow in the present simulation is thought to be safely within the two-dimensional regime [58–60]. The instantaneous vorticity and the dispersion of particle in the flow around an oscillating fiber are shown in Fig. 10. Alternating shedding vortices can be clearly found in the wake of the fiber as the flow Re is 100 (Fig. 10(a)). However, a relatively narrow width of the channel, i.e., $W/D = 3$ makes the vortexes interacting with each other in a short distance behind the fiber. From the particles dispersion pattern presented in Fig. 10(b), it is observed that the particles cannot enter into the vortex core zone, but are concentrated on the periphery of the vortex. This is because the aerodynamics response time of the particles is comparable to the characteristic time scale of the flow. Similar patterns of the vortex and particle dispersion have also been observed in Refs. [8,9]. Note that Fig. 10(b) also depicts the contours of the particle Reynolds number Re_p. The position for the emergence of larger Re_p locates at the front of fiber. Furthermore, particles at the periphery of the vortex do not always have larger Re_p as those for the case of stationary fiber [8], indicating that the motion of fiber can greatly reduce the slip velocity between the particle and gas. It is worth noting that in this case the maximum Re_p reaches as large as 1.3, for which the assumption of Stokes drag on the particle is no longer valid. Since the particle diameter is 147 nm ($St = 0.2$), corresponding to a Kn_p of $67/147 \approx 0.456$. Therefore, the influences of inertial and slip are both significant for the particle, and a correlation of drag force which combines those two effects should be adopted [51].

The distributions of the impact angle on the particle surface and the release position at the inlet along the vertical direction for the captured particles (the impact angle and release position are defined in Fig. 2) are shown in Fig. 11. From the comparisons of Fig. 11(a, b) with (c, d), it is seen that for low oscillation amplitude at $A/D = 0.1$, with the increase of the oscillation frequency, the shape of the distribution of impact angles is blunter, but the pattern of release positions becomes steeper. Similar phenomenon can also be found for larger $A/D = 0.4$ (Fig. 11(e, f, g, h)). The reason can be that the maximum velocity of the fiber is an increasing function of the frequency, which intensifies the flow field and then causes to broader particle dispersion on the fiber surface, the particles far from the inlet center, however will be squeezed away from the fiber. Moreover, it is observed that the distribution of the impact angle is generally unimodal and that of the release position is bimodal. However, decreasing A/D but increasing f/f_s generates the unimodal structure for the release position (Fig. 11(d)); bimodal structure for the impact angle emerges at larger A/D and f/f_s (Fig. 11(g)), and the range of the impact angle exceeds $[-90°, 90°]$, indicating a back-side impaction of the particles. In Ref. [10], Huagen et al. also found the back-side impaction for a stationary fiber with the flow Re larger than 1685. Obviously, oscillating motion of fiber is more prone to this phenomenon at a much lower Re.

Fig. 12 presents the collection efficiency η of a single oscillating fiber at different A/D and f/f_s for $St = 0.2$, 1.0 and 5.0. Generally, η is

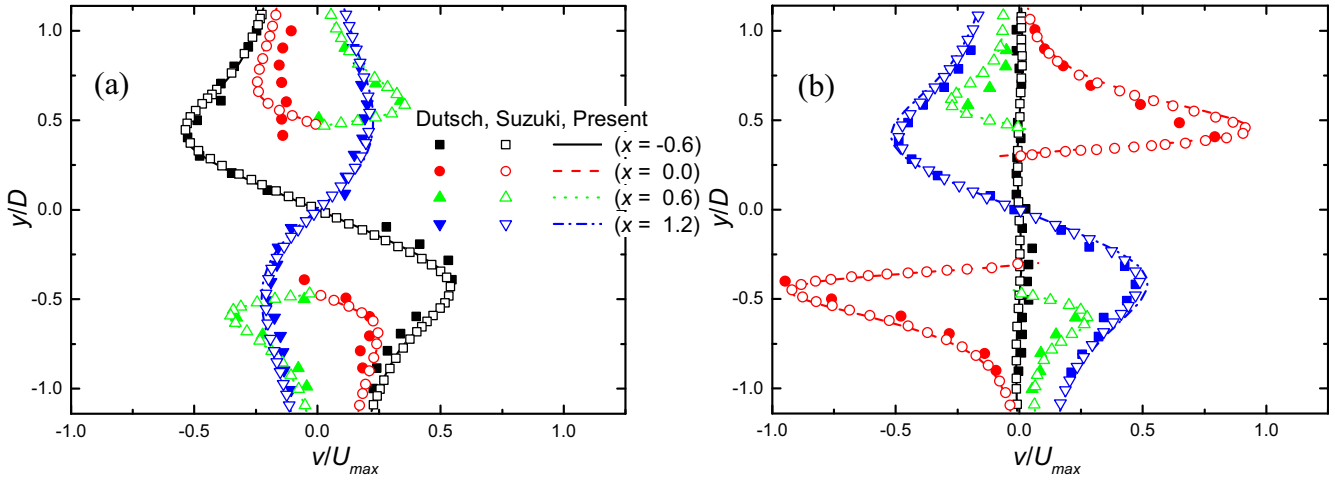

Fig. 8. Velocity profiles of the flow around an oscillating fiber at four locations $x = -0.6\ D$, 0, 0.6 D and 1.2 D for two phase angles $\phi = 210°$ (a) and 330° (b).

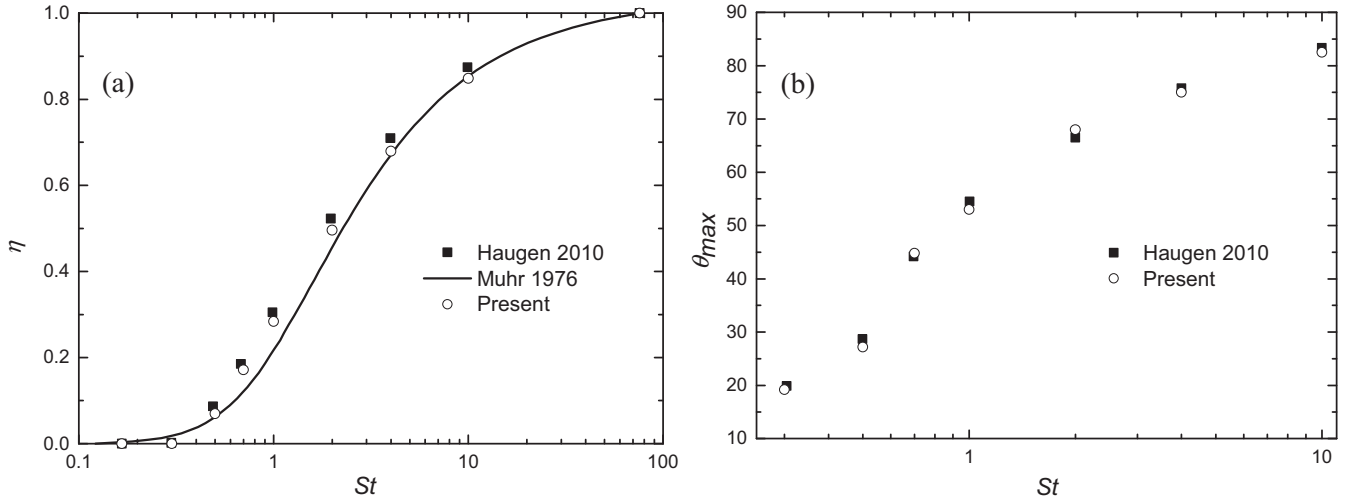

Fig. 9. (a) Collection efficiency of a single stationary fiber and (b) the maximum impact angle on the fiber surface as function of the Stokes number. The *St* here is calculated using the definition in Haugen et al. [10].

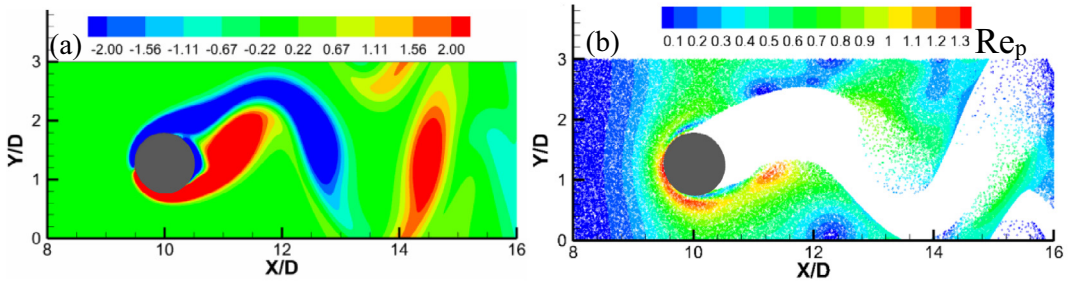

Fig. 10. (a) Instantaneous vorticity and (b) dispersion of particles in the flow around an oscillating fiber at $Re = 100$ with $St = 0.2$, $W/D = 3$, $A/D = 0.3$ and $f/f_s = 1.5$.

a linearly increasing function of both the A/D and f/f_s. In addition, the value of η is larger for larger St, but the increase rate of η calculated by $Slope/\eta_{(f/fs\ =\ 0.6)}$ decreases with the increase of St. This occurs since particle with larger St responds more slowly to the fluid motion due to larger inertia. However, particle with lower St are more sensitive to the fluid motion. It should be noted that at $A/D = 0.1$ for both $St = 1.0$ and 5.0, the η is almost independent of f/f_s. The results of η shown in Fig. 12(a, b, c) are transformed to be presented in Fig. 12(d) as a function of $(A/D \times f/f_s)$ which represents the maximum oscillating velocity of the fiber, $U_{max} = 2.0StrU_0A/Df/f_s$ with $Str = 0.167$ and $U_0 = 0.05$ fixed in the present study. It is observed that at lower St, η is almost linearly related with U_{max}, while some nonlinearity emerges in such relationship with increasing St.

4.1.2. Multiple fibers

To explore the influence of fiber number on the filtration performance of oscillating multi-fiber filter, N is increased from 1 to as large as 7 in this subsection. The other parameters are set as follows: $W/D = 3$, $L/D = 4$, $A/D = 0.3$ and $f/f_s = 1.5$ with St ranging from 0.06 to 10. Fig. 13(a) and (b) shows respectively the order of fiber obtaining the minimum and maximum collection efficiencies for $N = 2$–7. It can be found that the first fiber nearest to the inlet usually obtains the η_{min} at low $St \leq 0.2$ ($d_p \leq 147$ nm). This nontrivial phenomenon is opposite to that of the stationary multi-fiber filter case, where the first fiber has been reported to experience the η_{max} [28,13]. From the instantaneous vorticity, streamwise velocity and dispersion of particles, shown respectively in Fig. 14(a, b, c), vortex shedding can be clearly found between the first and second fiber, and the flow is greatly intensified. Therefore, the particle with relatively small inertia ($St \leq 0.2$) has the possibility to follow the flow, and easily slip over the first fiber and then approaches to the surface of the second fiber. For larger $St \geq 0.4$ ($d_p \geq 208$ nm), the filtration performance of the second fiber is being the worst, which is also not consistent with that of the stationary case [28]. This is because the second fiber is shielded by the first one and then inertial particles can be hardly entrained to its surface as shown in Fig. 14(d), while the particle can still be fed to the region behind the second fiber. It is noted that the third fiber may perform the worst at $St \geq 0.2$ and $N \geq 5$ in several situations. As for the fiber obtaining the η_{max} depicted in Fig. 13(b), it is interesting to observe that the last fiber closest to the outlet performs the best for smaller particles. With the increase of St this number moves down, and eventually collapses to 1 for $St \geq 4.0$. Particularly, a transition state emerges at $N \geq 5$ that the second one nearest to the outlet performs the best in the intermediate St range. For example, at $N = 6$, this range is $0.1 \leq St \leq 1.0$.

It is of importance to analysis which vertical position at the inlet that the released particle is more likely to be captured, and which portion of the fiber surface is more vulnerable to the impaction of particles. Fig. 15(a) and (c) then show the distributions of the impact angle for captured particles at $N = 4$ with $St = 0.2$ and 6.0, respectively. Fiber with different order (counting from the inlet to outlet) usually has different distribution of the impact angle. Generally, the first fiber has a unimodal pattern. This is because the fiber is under low-intensity oscillating motion with $A/D = 0.3$ and $f/f_s = 1.5$ so that it hardly impacts the flow in front of the fiber. The second fiber is shielded directly by the first fiber, so that the

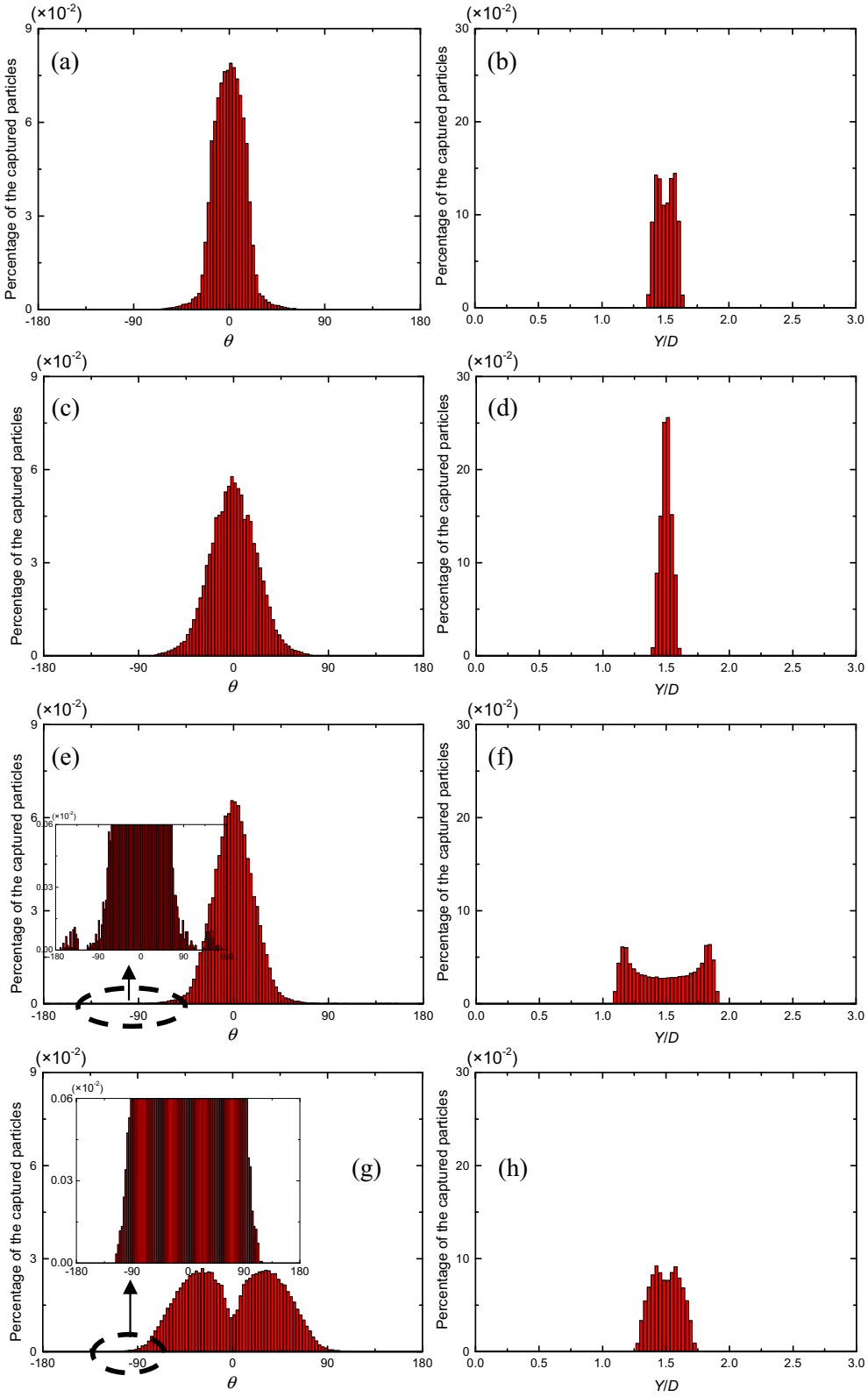

Fig. 11. Distributions of the impact angle on the fiber surface (left column) and the release position at the inlet along the vertical direction (right column) for the captured particles with $St = 0.2$, $A/D = 0.1$: $f/f_s = 0.6$ (a, b), 2.5 (c, d); $St = 0.2$, $A/D = 0.4$: $f/f_s = 0.6$ (e, f), 2.5 (g, h). (i) is the streamwise velocity with $A/D = 0.4$ and $f/f_s = 0.6$.

fluid mainly moves along the two lateral sides of the second fiber, resulting in a bimodal pattern (Fig. 15(a, c)). As the fluid flows continually past the second fiber, it is fully intensified and more complex pattern of the impact angle can be found at the surface of the third and fourth fibers. The distributions of the release position for the captured particles are presented in Fig. 15(b) and (d) at $St = 0.2$ and 6.0 respectively. Different from the single oscillating fiber case ($N = 1$, Fig. 11), particles across the inlet all

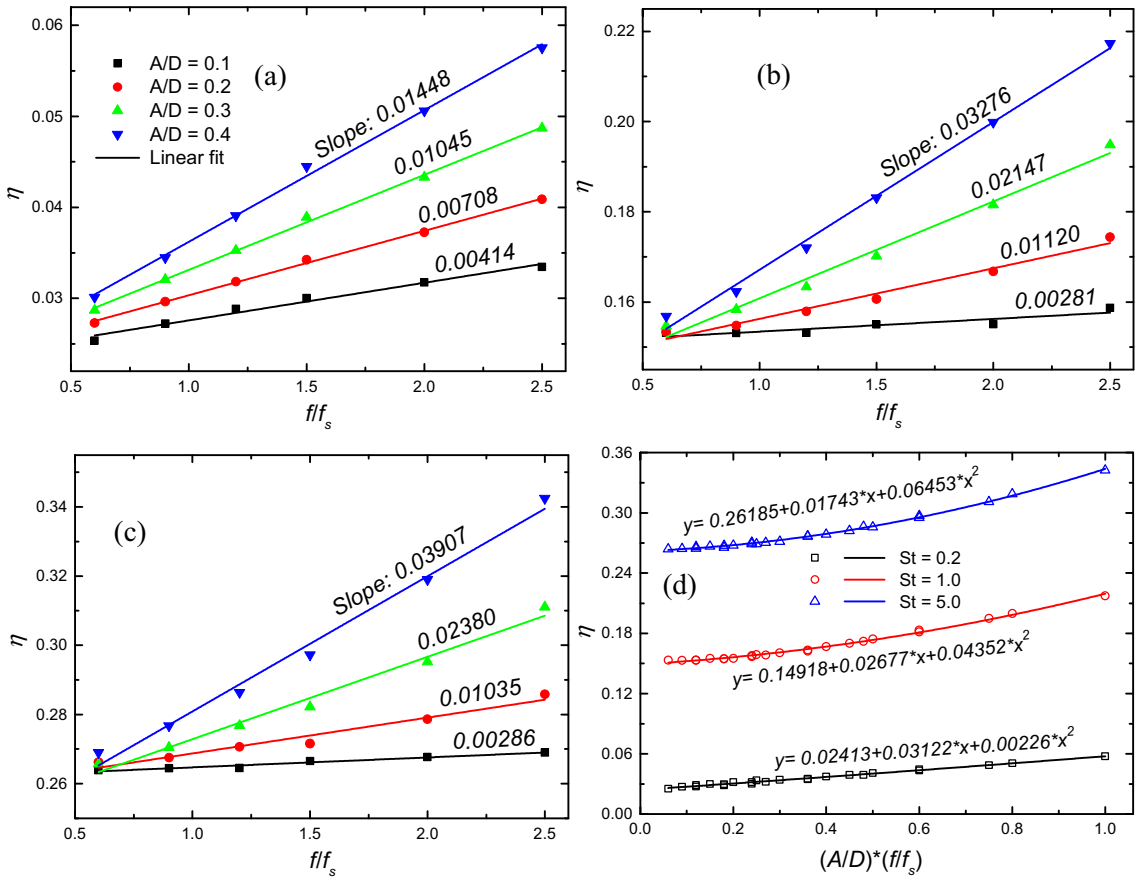

Fig. 12. Collection efficiency η of a single oscillating fiber with different A/D and f/f_s: (a) St = 0.2; (b) St = 1.0; (c) St = 5.0. The results of η are redrawn as a function of $(A/D \times f/f_s)$ (d).

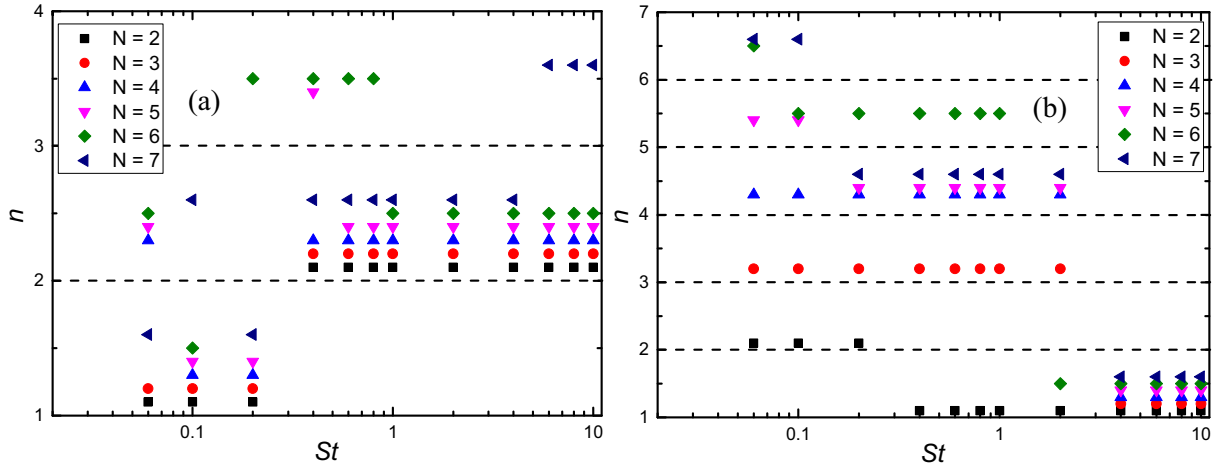

Fig. 13. The order of fiber n that obtains the minimum (a) and maximum (b) collection efficiencies at different St for N = 2–7. Note that n in the figures is shown for clarity and its actual value should be rounded down.

have a high possibility to be captured by the multi-fiber filter. Particularly, for smaller particles (St = 0.2, d_p = 147 nm), local extremes emerge at several positions, and the vertical center is not always the location where the released particle is most likely to be captured.

The collection efficiency at different St for multi-fiber filters with N = 2–7 is shown in Fig. 16. For each fiber number, η is generally increases rapidly first and then slowly for a threshold St about 1.0. This feature is similar to that of a single stationary fiber case [9]. Note that a short descent process of η when St > 4.0 for N = 3 can be found, indicating a more complicated flow-fiber-particle interaction in the oscillating multi-fiber filter. Moreover, η is larger with increasing N, and especially it is substantially enhanced when N changes from 2 to 4. The variation of η is, however, almost independent of the fiber number until N reaches 7 and St > 1.0. Therefore, it can be concluded that the filtration performance of

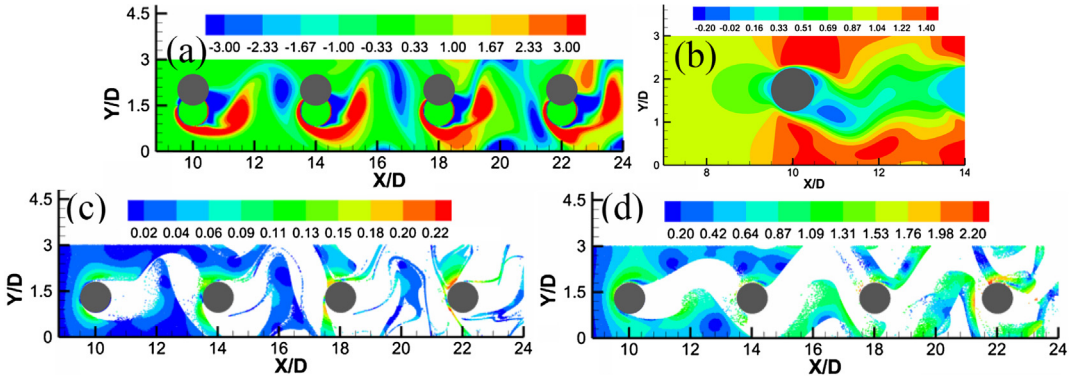

Fig. 14. The instantaneous vorticity (a), streamwise velocity (b), dispersion of particles at $St = 0.2$ (c) and dispersion of particles at $St = 6.0$ (d) with $N = 4$, $W/D = 3$, $L/D = 4$, $A/D = 0.3$ and $f/f_s = 1.5$.

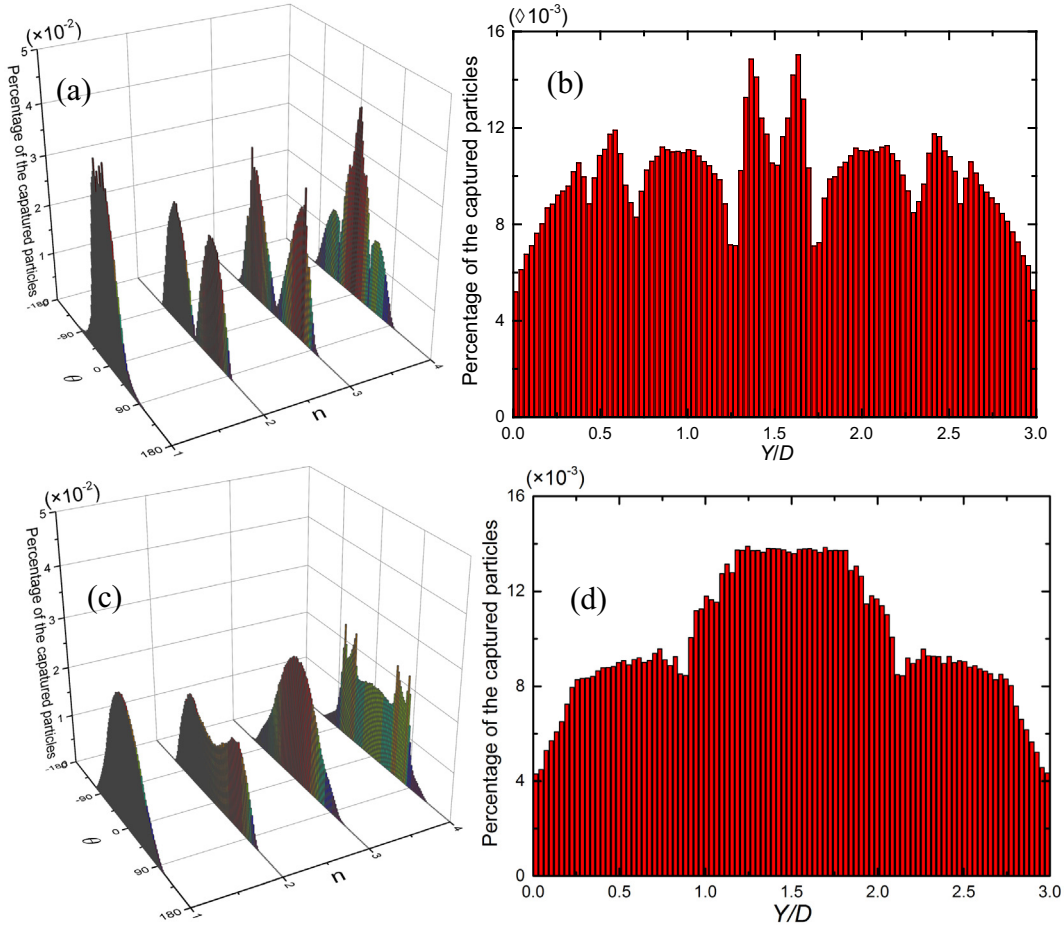

Fig. 15. The distributions of the impact angle on each fibers and the release position at $St = 0.2$(a, b) and $St = 6.0$ (b, d) respectively, with $N = 4$, $W/D = 3$, $L/D = 4$, $A/D = 0.3$ and $f/f_s = 1.5$.

oscillating multi-fiber filter cannot be represented by the single oscillating fiber model.

4.2. Effect of fiber arrangement

In this subsection, the influence of the fiber arrangement, mainly governed by the separation ratios longitudinally L/D and transversely W/D, on the filtration performance is investigated. L/D is varied from 2 to 6, and W/D from 2 to 4. As a representative of multi-fiber filter, the number of fibers is fixed at $N = 4$. The fibers are all under in-phase motion with the amplitude $A/D = 0.3$ and frequency $f/f_s = 1.5$. Three particle sizes with $St = 0.2$, 1.0 and 5.0 are considered, corresponding to d_p of 147 nm, 329 nm, and 736 nm, respectively. It is known that the particle-laden flow in the multi-fiber filter can be significantly changed with the variation in the arrangement of stationary fibers [13,14]. For the oscillating multi-fiber filter, the dispersion of particles with different fibers arrangement is presented in Fig. 17. It is observed clearly that with the increase of the longitudinal spacing L/D, the flow is intensified and the particles can be introduced into the region between the

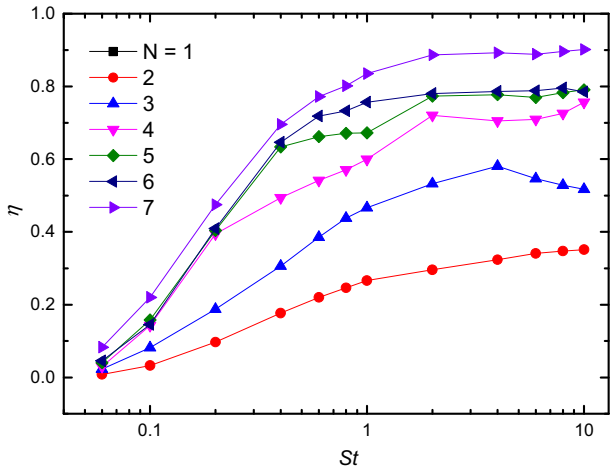

Fig. 16. Collection efficiency at different *St* for multi-fiber filters with *N* = 2–7.

fibers, as shown in Fig. 17(b, d). This will definitely affect the collection efficiency of fibers behind the first fiber. However, increasing the transverse spacing *W*/*D* (Fig. 17(a, c)) only has a minor effect on the flow field, and the fibers behind the first one remain shielded. It is also interesting to find that two strands of particles can escape capture by the fibers in the case shown in Fig. 17(c, d). While *W*/*D* is increased, those particles can still slip over the first and second fibers, but could deposit on the three and four fibers (Fig. 17(d)). These observations are consistent with the results given in Fig. 18.

Fig. 19 presents the collection efficiency η under different arrangement of the fibers for *St* = 0.2, 1.0 and 5.0. For a constant *St*, η is generally a decreasing function of *W*/*D*, especially for small or large *L*/*D*. However, exception occurs under the situation of narrow channel when comparing the cases of *W*/*D* = 2 and *W*/*D* = 3 at *L*/*D* = 4 and *St* = 0.2, as shown in Fig. 19(a). From the results of the collection efficiency of each fiber shown in Fig. 20, the main contribution of the larger η at *W*/*D* = 3 is found to ascribe to a dramatic increase of η for the fourth fiber. The relationship between η and *L*/*D* fluctuates at small *W*/*D*, while for large *W*/*D*, it increases first and then decreases later.

4.3. Effect of fiber vibration parameters

4.3.1. Vibration amplitude

The first parameter that controls the oscillating motion of fiber is the amplitude ratio *A*/*D*. To examine its influence on the filtration performance for the case of multiple fibers, a set of simulations with *A*/*D* ranging from 0.1 to 0.5 with *N* = 4, *W*/*D* = 3, *L*/*D* = 4 and f/f_s = 1.5 are conducted. The collection efficiency η generally shows the non-monotonic behaviors, i.e., reduction-augmentation- reduction with the increase of *A*/*D* for *St* ≥ 1.0, as depicted in Fig. 21. The local minimum and maximum values occur at *A*/*D* = 0.2 and 0.3, respectively. Exception appears for larger particle (*St* = 5.0, d_p = 736 nm) where η continues to increase slowly for *A*/*D* ≥ 0.4. For smaller particles (*St* = 0.2, d_p = 147 nm), within the ranges of *A*/*D* ≥ 0.4 and *A*/*D* ≤ 0.2, the variation of η is rather small. It is interesting to note that at larger *St* = 5.0, η is smaller than that of lower *St* = 1.0 when the vibration amplitude is small (*A*/*D* = 0.1). To explain this phenomenon, the collection efficiency for individual fibers at *A*/*D* = 0.1 for *St* = 1.0 and 5.0 is shown in Fig. 22. It is found that, compared to the case of *St* = 5.0, the relative increase in η for the third fiber is larger than the relative decrease for the first fiber at *St* = 1.0.

4.3.2. Vibration frequency

The second control parameter for the fiber motion is the normalized frequency f/f_s, and it ranges from 0.6 to 2.5 in this subsection with *N* = 4, *W*/*D* = 3, *L*/*D* = 4 and *A*/*D* = 0.3. Fig. 23 shows the collection efficiency η at different f/f_s for *St* = 0.2, 1.0 and 5.0. When the particle is small (*St* = 0.2, d_p = 147 nm) or large (*St* = 5.0, d_p = 736 nm), the general trend is that η increases first and then descends with the increase of f/f_s. The local maximum values emerge at around f/f_s = 1.5 and 0.9, for *St* = 0.2 and 5.0, respectively, indicating a lower optimal frequency for lager particles. Therefore, to achieve a better filtration performance, the vibration frequency of the fibers should not be too large for large particles. For the intermediate case, i.e., *St* = 1.0 (d_p = 329 nm), there are two local maximum values of η. Generally, the influence of frequency on the filtration performance is a bit complicated for particles with moderate size. To explore the effect of frequency on the individual fibers, the collection efficiency of each fiber is displayed in Fig. 24 for f/f_s = 1.2, 1.5 and 2.0 at *St* = 0.2. It is found that the first fiber performs the worst while the last fiber performs the best, respectively, for this range of f/f_s.

4.3.3. In-phase and anti-phase

Apart from the influence of amplitude and frequency of the oscillating motion of fiber, the fibers may vibrate in-phase or anti-phase when multiple fibers are considered in the present study. The simulations conducted above only address the in-phase case. Hence, three situations of anti-phase are investigated next, for the multi-fiber filter with *N* = 4, as depicted in Fig. 25(b, c, d), where two of the four fibers move initially in the opposite direction for the other two fibers. The remaining parameters are set to be *W*/*D* = 3, *L*/*D* = 4, *A*/*D* = 0.3 and f/f_s = 1.5.

The collection efficiency η at different *St* for the four vibration modes is presented in Fig. 26. It is observed that, fortunately,

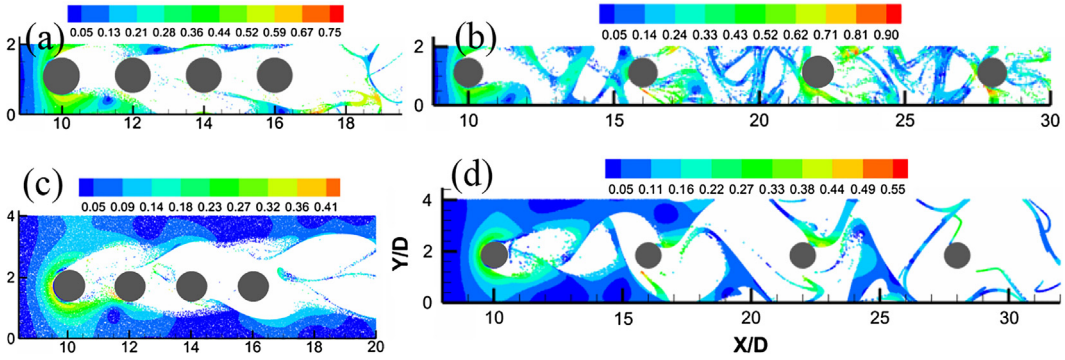

Fig. 17. Dispersion of the particles at different arrangement of fibers for *St* = 1.0. (a): *W*/*D* = 2, *L*/*D* = 2; (b): *W*/*D* = 2, *L*/*D* = 6; (c): *W*/*D* = 4, *L*/*D* = 2; (d): *W*/*D* = 4, *L*/*D* = 6.

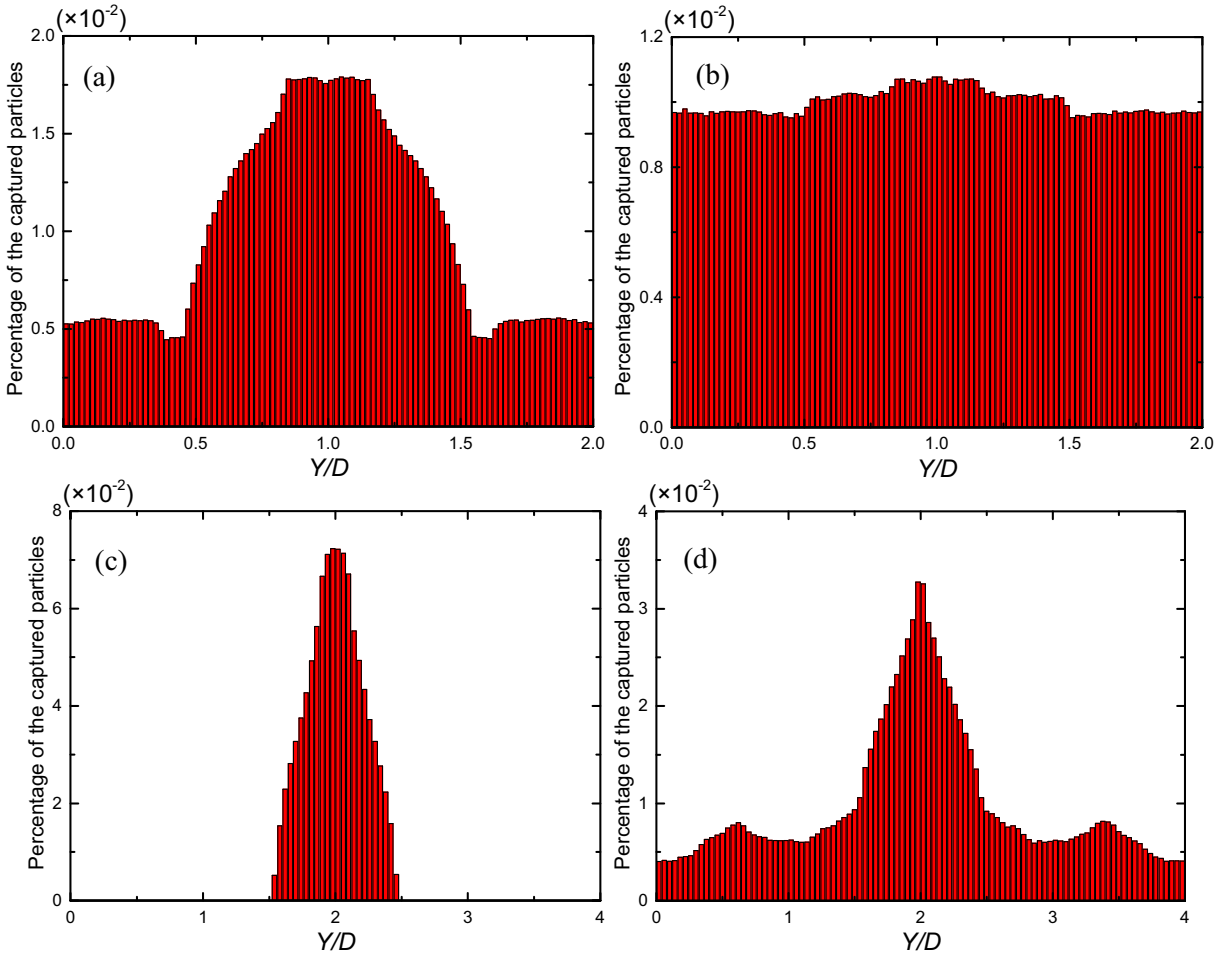

Fig. 18. The distribution of the release position at different arrangement of fibers for St = 1.0. (a): W/D = 2, L/D = 2; (b): W/D = 2, L/D = 6; (c): W/D = 4, L/D = 2; (d): W/D = 4, L/D = 6.

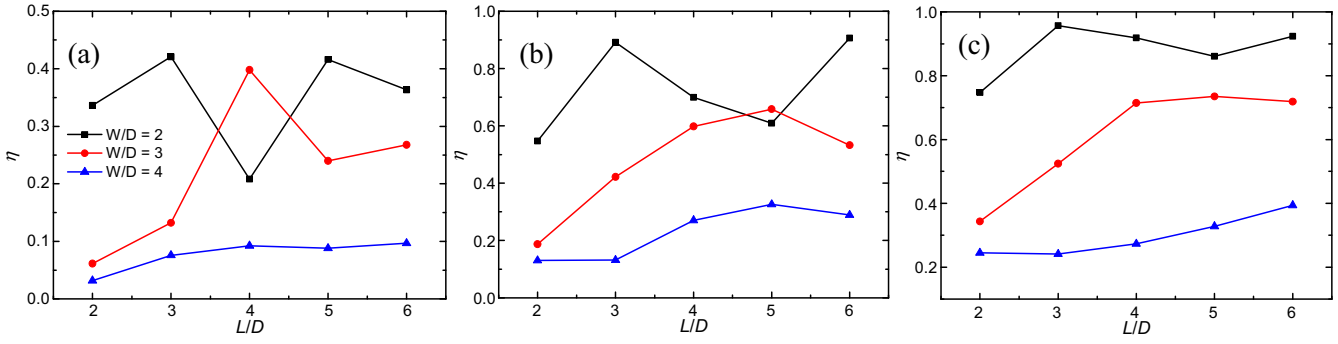

Fig. 19. Collection efficiency at different longitudinal spacing L/D and transverse spacing W/D for (a) St = 0.2, (b) St = 1.0, and (c) St = 5.0.

Mode 1, i.e., the four fibers being in-phase vibration, can generally achieve the excellent filtration performance, especially for the fine particles (St = 0.2, d_p = 147 nm). This corresponds to a simpler way to control the motion of fibers in practice. Moreover, as already known from the results at N = 4 in Fig. 13, small particle is able to avoid capture by the first fiber and the last fiber plays significant role in filtration at St = 0.2 for Mode 1. However, from the collection efficiency of each fiber shown in Fig. 27, the first fiber is still not so significant, but the fourth fiber tends to perform the worst in Mode 3. It is interesting to observe that η increases rapidly with St for Mode 3, and eventually it is comparable with that of Mode 1 at St = 5.0 (Fig. 26). That is attributed to the contribution of the third fiber as particles can always be efficiently captured by this fiber (Fig. 27). Because of the phase difference between the first two and the last two fibers (Fig. 25 (c)) in Model 3, particles slipping over the first and second fibers will deposit on the third fiber. Obviously, the filtration feature for individual fibers established in the Section 4.1.2 (Fig. 13) not holds when the fibers are in the anti-phase vibration, as shown in Fig. 27.

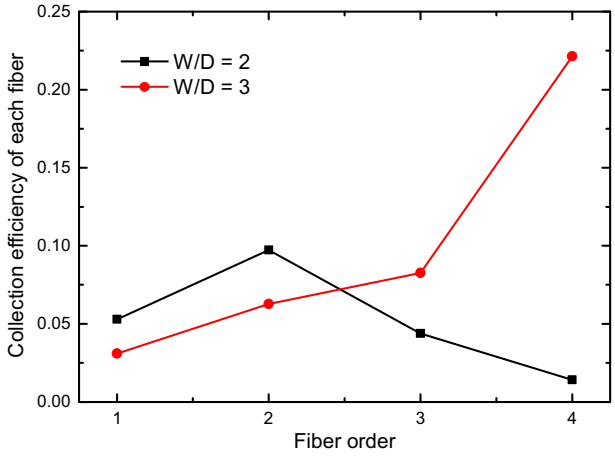

Fig. 20. Collection efficiency for individual fibers at $W/D = 2$ and 3 at $L/D = 4$ for $St = 0.2$.

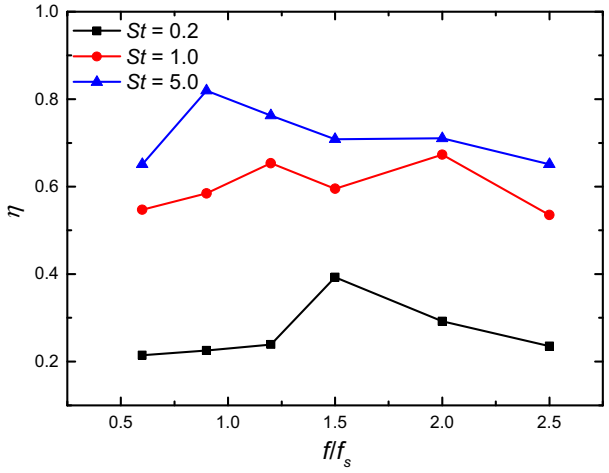

Fig. 23. Collection efficiency at different frequency ratio f/f_s for $St = 0.2$, 1.0 and 5.0.

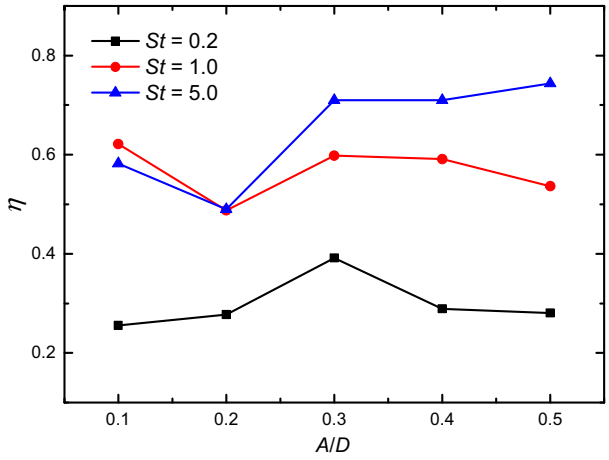

Fig. 21. Collection efficiency at different amplitude A/D for $St = 0.2$, 1.0 and 5.0.

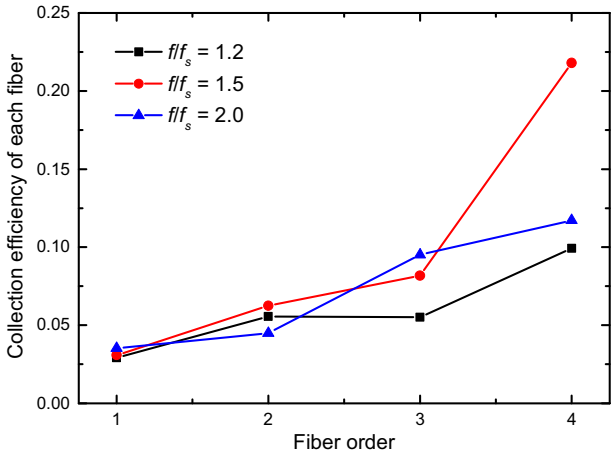

Fig. 24. Collective efficiency for individual fibers at $St = 0.2$ for $f/f_s = 1.2$, 1.5 and 2.0.

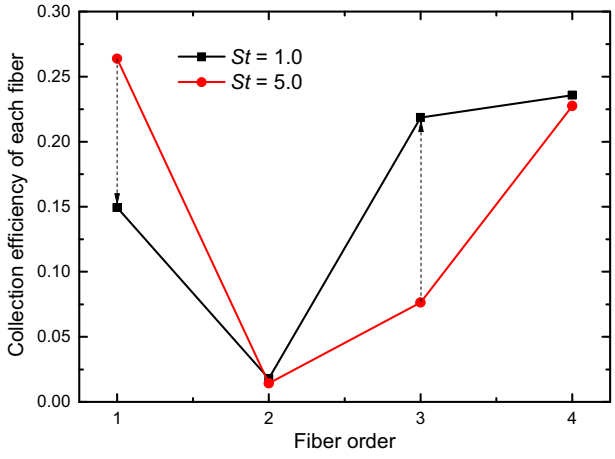

Fig. 22. Collection efficiency for individual fibers at $A/D = 0.1$ with $St = 1.0$ and 5.0.

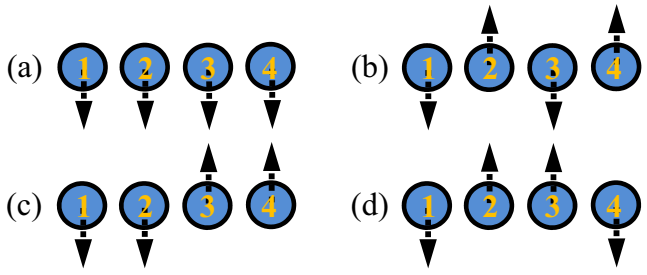

Fig. 25. Sketch of the four vibration models for the fibers with initial motion direction. (a): in-phase; (b) to (d): anti-phase.

5. Conclusions

The dispersion and deposition of dilute aerosol particles entrained in a gas flow through an oscillating multi-fiber filter is investigated numerically. The gas flow with moving fibers is solved using an efficient iterative immersed boundary-lattice Boltzmann method, where the no-slip boundary condition can be exactly enforced with an iterative approach and the numerical stability is improved by adopting the MRT collision model. The one-way coupling Lagrangian approach is applied to track the aerosol particles. The ability of the model, i.e., the iterative IB-LBM coupled with the Lagrangian approach in handling the particle-laden flows through the complex passage has been demonstrated in two test cases designed to validate the accuracy of the immersed boundary method for a moving fluid-solid interface and the Lagrangian approach for particle dispersion and deposition, respectively.

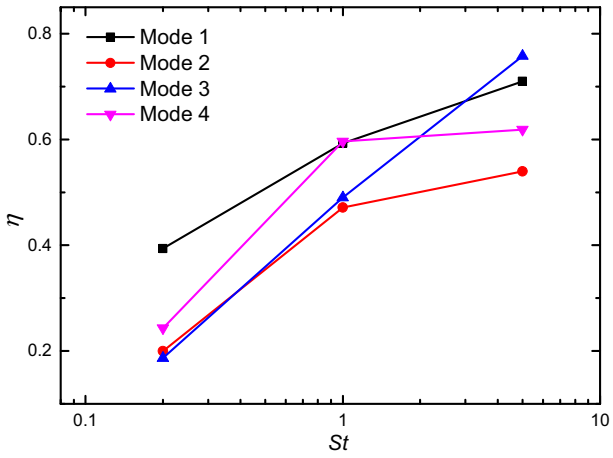

Fig. 26. Collection efficiency at different *St* for the four vibration modes.

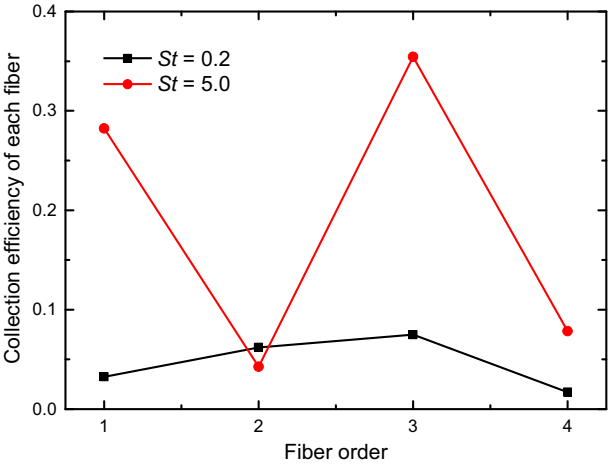

Fig. 27. Collection efficiency for individual fibers at *St* = 0.2 and 5.0 in Mode 3.

In the simulations of particle transport and deposition through a fibrous filter, necessary model simplifications are made and limited ranges of a few model parameters are considered. The flow Reynolds number is fixed at *Re* = 100, and the particle Stokes number ranges from *St* = 0.06–10.0. The effects of the fiber number, fiber arrangement parameters, and fiber vibration mode are studied in detail. Our numerical results show that the oscillating motion of fibers has a significant influence on the filtration performance. Specifically, the following conclusions can be drawn.

For the case of a single fiber, the distribution ranges of the release position and impaction angle for captured particles both increase with the vibration amplitude, while these two ranges decrease and increase, respectively, with the increase in the vibration frequency. At larger amplitude and frequency, the distribution pattern of the impact angle changes from a unimodal to bimodal shape, and the back-side impaction deposition emerges. Furthermore, a linear relationship can be generally found between the collection efficiency and the vibration amplitude or frequency.

For the case of multiple fibers, the collection efficiency always increases with the number of fibers in the passage. However, the dependence of the collection efficiency on the separation ratios, longitudinally and transversely in the fiber arrangement, and the parameters for oscillating motion of fiber, i.e., the amplitude and frequency, is complex and non-monotonic. It is interesting to find that the in-phase vibration mode can generally lead to excellent collection efficiency.

The present study only considers straight and uniform-distributed circular fibers, and dilute particle flows. Note that the fibers can be in staggered arrangements, and have irregular shape in actual applications. The fibers may have deformation along the length, and hence the elongation affects the collection efficiency of the filter where three-dimensional simulation should be conducted. Furthermore, for some particle flows, the interactions of fluid-particle and particle-particle should be well considered. Those effects will be studied in the future work.

Acknowledgements

This work is subsidized by the National Natural Science Foundation of China (51390494). L.P. Wang acknowledges the support of the U.S. National Science Foundation under grants CNS-1513031, CBET-1235974, and AGS-1139743.

Conflict of interest

The authors have declared that no conflict of interest exists.

References

[1] S. Li, J.S. Marshall, G. Liu, Q. Yao, Adhesive particulate flow: The discrete-element method and its application in energy and environmental engineering, Prog. Energy Combust. Sci. 37 (6) (2011) 633–668.
[2] C.S. Wang, Y. Otani, Removal of nanoparticles from gas streams by fibrous filters: a review, Ind. Eng. Chem. Res. 52 (1) (2012) 5–17.
[3] S.Q. Li, J.S. Marshall, Discrete element simulation of micro-particle deposition on a cylindrical fiber in an array, J. Aerosol Sci. 38 (10) (2007) 1031–1046.
[4] N.L. Mills, K. Donaldson, P.W. Hadoke, N.A. Boon, W. MacNee, F.R. Cassee, T. Sandström, A. Blomberg, D.E. Newby, Adverse cardiovascular effects of air pollution, Nat. Clin. Pract. Cardiovasc Med. 6 (1) (2009) 36–44.
[5] J. Liu, S.Q. Jin, W.B. Yuan, X.D. Xiang, Gas-liquid separation mechanism and experimental study of wet vibrating grid precipitator, J. WUHAN Univ. Techol. 4 (2013) 014.
[6] Y.H. Zhang, J. Liu, Z.A. Huang, Y.K. Gao, The performance optimization experiment of a wet high-frequency vibrating grid, in: Proc. 3rd International Symposium on Mine Safety Science and Engineering, Montreal, Canada, 2016, COLL–268.
[7] D.J. Brandon, S.K. Aggarwal, A numerical investigation of particle deposition on a square cylinder placed in a channel flow, Aerosol Sci. Technol. 34 (4) (2001) 340–352.
[8] J. Yao, Y. Zhao, G. Hu, J. Fan, K. Cen, Numerical simulation of particle dispersion in the wake of a circular cylinder, Aerosol Sci. Technol. 43 (2) (2009) 174–187.
[9] S. Jafari, M. Salmanzadeh, M. Rahnama, G. Ahmadi, Investigation of particle dispersion and deposition in a channel with a square cylinder obstruction using the lattice Boltzmann method, J. Aerosol Sci. 41 (2) (2010) 198–206.
[10] N.E.L. Haugen, S. Kragset, Particle impaction on a cylinder in a crossflow as function of Stokes and Reynolds numbers, J. Fluid Mech. 661 (2010) 239–261.
[11] D. Shou, J. Fan, H. Zhang, X. Qian, L. Ye, Filtration efficiency of non-uniform fibrous filters, Aerosol Sci. Technol. 49 (10) (2015) 912–919.
[12] Z.G. Liu, P.K. Wang, Pressure drop and interception efficiency of multifiber filters, Aerosol Sci. Technol. 26 (4) (1997) 313–325.
[13] K.C. Lin, H. Tao, K.W. Lee, An early stage of aerosol particle transport in flows past periodic arrays of clear staggered obstructions: A computational study, Aerosol Sci. Technol. 48 (12) (2014) 1299–1307.
[14] W. Li, S. Shen, H. Li, Study and optimization of the filtration performance of multi-fiber filter, Adv. Powder Technol. 27 (2) (2016) 638–645.
[15] D. Shou, J. Fan, L. Ye, H. Zhang, X. Qian, Z. Zhang, Inverse problem of air filtration of nanoparticles: optimal quality factors of fibrous filters, J. Nanomater. 16 (1) (2015) 351.
[16] D. Timerman, D.F. Greene, J. Urzay, J.D. Ackerman, Turbulence-induced resonance vibrations cause pollen release in wind-pollinated Plantagolanceolata L. (Plantaginaceae), J. R. Soc. Interface 11 (101) (2014) 20140866.
[17] K. Ecord, L.A. Glasgow, Vortex-enhanced capture of airborne particulates, Environ. Technol. 23 (2) (2002) 217–226.
[18] S. Khorasanizade, J.M.M. Sousa, Using a fully-Lagrangian meshless method for the study of aerosol dispersion and deposition, Aerosol Sci. Technol. 50 (9) (2016) 926–936.
[19] J.I. Holmes, L.A. Glasgow, Capture of airborne particles using intensified vortices, Part. Sci. Technol. 2 (3) (2006) 259–269.
[20] P.N. Price, A.J. Gadgil, M.D. Sohn, Trade-offs between moving and stationary particle collectors for detecting a bio-agent plume, Atmos. Environ. 41 (38) (2007) 8818–8824.
[21] R. Mead-Hunter, A.J. King, A.N. Larcombe, B.J. Mullins, The influence of moving walls on respiratory aerosol deposition modeling, J. Aerosol Sci. 64 (2013) 48–59.

[22] J. Krick, J.D. Ackerman, Adding ecology to particle capture models: Numerical simulations of capture on a moving cylinder in crossflow, J. Theor. Biol. 368 (2015) 13–26.
[23] B. Liu, W. Zhou, P. Tan, X. Shan, Q. Yang, Dynamic granular bed and its gas-solid separation process, Powder Technol. 301 (2016) 387–395.
[24] Y.S. Chen, S.S. Hsiau, C.J. Hsu, S.M. Ma, Y.L. Chang, Influence of operational parameters on the performance of gas clean-up technology with a moving granular bed filter, Energy 139 (2017) 842–852.
[25] Y.S. Chen, C.J. Hsu, S.S. Hsiau, S.M. Ma, Clean coal technology for removal dust using moving granular bed filter, Energy 120 (2017) 441–449.
[26] Z. Guo, C. Shu, Lattice Boltzmann Method and its Applications in Engineering, World Scientific, Singapore, 2013.
[27] Y.H. Qian, D. d'Humières, P. Lallemand, Lattice BGK models for Navier-Stokes equation, Europhys. Lett. 17 (6) (1992) 479.
[28] H. Wang, H. Zhao, K. Wang, Y. He, C. Zheng, Simulation of filtration process for multi-fiber filter using the Lattice-Boltzmann two-phase flow model, J. Aerosol Sci. 66 (2013) 164–178.
[29] L. Ding, A.C.K. Lai, An efficient lattice Boltzmann model for indoor airflow and particle transport, J. Aerosol Sci. 63 (2013) 10–24.
[30] G. Wu, Z. Miao, W.J. Jasper, A.V. Kuznetsov, Modeling of submicron particle filtration in an electret monolith filter with rectangular cross-section microchannels, Aerosol Sci. Technol. 50 (10) (2016) 1033–1043.
[31] A.J.C. Ladd, R. Verberg, Lattice-Boltzmann simulations of particle-fluid suspensions, J. Stat. Phys. 104 (5–6) (2001) 1191–1251.
[32] Z.G. Feng, E.E. Michaelides, The immersed boundary-lattice Boltzmann method for solving fluid-particles interaction problems, J. Comput. Phys. 195 (2) (2004) 602–628.
[33] M. Habte, C. Wu, Particle sedimentation using hybrid Lattice Boltzmann-immersed boundary method scheme, Powder Technol. 315 (2017) 486–498.
[34] S. Tao, J. Hu, Z. Guo, An investigation on momentum exchange methods and refilling algorithms for lattice Boltzmann simulation of particulate flows, Comput. Fluids 133 (2016) 1–14.
[35] C. Peng, Y. Teng, B. Hwang, Z. Guo, L.P. Wang, Implementation issues and benchmarking of lattice Boltzmann method for moving rigid particle simulations in a viscous flow, Comput. Math. Appl. 72 (2) (2016) 349–374.
[36] K. Luo, Z. Wang, J. Fan, K. Cen, Full-scale solutions to particle-laden flows: Multidirect forcing and immersed boundary method, Phys. Rev. E 76 (6) (2007) 066709.
[37] M.R. Maxey, J.J. Riley, Equation of motion for a small rigid sphere in a nonuniform flow, Phys. Fluids 26 (4) (1983) 883–889.
[38] T.L. Hoffmann, G.H. Koopmann, Visualization of acoustic particle interaction and agglomeration: Theory and experiments, J. Acoust. Soc. Am. 99 (4) (1996) 2130–2141.
[39] J.A. Hubbard, J.E. Brockmann, J. Dellinger, D.A. Lucero, A.L. Sanchez, B.L. Servantes, Fibrous filter efficiency and pressure drop in the viscous-inertial transition flow regime, Aerosol Sci. Technol. 46 (2) (2012) 138–147.
[40] Y. Otani, K. Eryu, M. Furuuchi, N. Tajima, P. Tekasakul, Inertial classification of nanoparticles with fibrous filters, Aerosol Air Qual. Res. 7 (2007) 343–352.
[41] Q. Du, L. Su, H. Dong, J. Gao, Z. Zhao, D. Lv, S. Wu, The experimental study of a water-saving wet electrostatic precipitator for removing fine particles, J. Electrostat. 81 (2016) 42–47.
[42] P. Lallemand, L.S. Luo, Theory of the lattice Boltzmann method: Dispersion, dissipation, isotropy, Galilean invariance, and stability, Phys. Rev. E 61 (6) (2000) 6546.
[43] Y. Guan, R. Guadarrama-Lara, X. Jia, K. Zhang, D. Wen, Lattice Boltzmann simulation of flow past a non-spherical particle, Adv. Powder Technol. 28 (6) (2017) 1486–1494.
[44] Z. Guo, C. Zheng, B. Shi, Discrete lattice effects on the forcing term in the lattice Boltzmann method, Phys. Rev. E 65 (4) (2002) 046308.
[45] C.S. Peskin, Flow patterns around heart valves: a numerical method, J. Comput. Phys. 10 (2) (1972) 252–271.
[46] R. Mittal, G. Iaccarino, Immersed boundary methods, Annu. Rev. Fluid Mech. 37 (2005) 239–261.
[47] H.H. Afrouzi, M. Farhadi, A.A. Mehrizi, Numerical simulation of microparticles transport in a concentric annulus by Lattice Boltzmann Method, Adv. Powder Technol. 24 (3) (2013) 575–584.
[48] L. Schiller, A. Naumann, Über die grundlegendenBerechnungenbei der Schwerkraftaufbereitung, Z. Ver. Dtsch. Ing. 77 (12) (1933) 318–320.
[49] N.V. Koralkar, M. Bose, Performance of drag models for simulation of fluidized beds with Geldart D particles, Adv. Powder Technol. 27 (6) (2016) 2377–2398.
[50] M.D. Allen, O.G. Raabe, Slip correction measurements of spherical solid aerosol particles in an improved Millikan apparatus, Aerosol Sci. Technol. 4 (3) (1985) 269–286.
[51] S. Tao, H. Zhang, Z. Guo, Drag correlation for micro spherical particles at finite Reynolds and Knudsen numbers by lattice Boltzmann simulations, J. Aerosol Sci. 103 (2017) 105–116.
[52] A. Li, G. Ahmadi, Dispersion and deposition of spherical particles from point sources in a turbulent channel flow, Aerosol Sci. Technol. 16 (4) (1992) 209–226.
[53] H. Dütsch, F. Durst, S. Becker, H. Lienhart, Low-Reynolds-number flow around an oscillating circular cylinder at low Keulegan-Carpenter numbers, J. Fluid Mech. 360 (1998) 249–271.
[54] K. Suzuki, T. Inamuro, Effect of internal mass in the simulation of a moving body by the immersed boundary method, Comput. Fluids 49 (1) (2011) 173–187.
[55] G.H. Koopmann, The vortex wakes of vibrating cylinders at low Reynolds numbers, J. Fluid Mech. 28 (3) (1967) 501–512.
[56] C.S. Peskin, The immersed boundary method, Acta Numer. 11 (2002) 479–517.
[57] W. Muhr, Theoretical and experimental investigation of particle deposition in fibrous filters by field and inertial forces, Doctoral dissertation, Institutfür Mechanische Verfahrenstechnik und Mechanik, Universität Karlsruhe, Karlsruhe, Germany, 1976.
[58] J.S. Leontini, M.C. Thompson, K. Hourigan, Three-dimensional transition in the wake of a transversely oscillating cylinder, J. Fluid Mech. 577 (2007) 79–104.
[59] E. Berger, Suppression of vortex shedding and turbulence behind oscillating cylinders, Phys. Fluids 10 (9) (1967) 191–193.
[60] M. Tatsuno, P.W. Bearman, A visual study of the flow around an oscillating circular cylinder at low Keulegan-Carpenter numbers and low Stokes numbers, J. Fluid Mech. 211 (1990) 157–182.